Since January 2020 Elsevier has created a COVID-19 resource centre with free information in English and Mandarin on the novel coronavirus COVID-19. The COVID-19 resource centre is hosted on Elsevier Connect, the company's public news and information website.

Environment International 150 (2021) 106426

Contents lists available at ScienceDirect

Environment International

journal homepage: www.elsevier.com/locate/envint

Impacts of primary emissions and secondary aerosol formation on air pollution in an urban area of China during the COVID-19 lockdown

Jie Tian [a,b,c], Qiyuan Wang [a,b,c,*], Yong Zhang [a], Mengyuan Yan [d], Huikun Liu [a], Ningning Zhang [a], Weikang Ran [a], Junji Cao [a,b,c,*]

[a] Key Laboratory of Aerosol Chemistry and Physics, State Key Laboratory of Loess and Quaternary Geology, Institute of Earth Environment, Chinese Academy of Sciences, Xi'an 710061, China
[b] CAS Center for Excellence in Quaternary Science and Global Change, Xi'an 710061, China
[c] Shaanxi Key Laboratory of Atmospheric and Haze-fog Pollution Prevention, Xi'an 710061, China
[d] School of Human Settlements and Civil Engineering, Xi'an Jiaotong University, Xi'an 710049, China

ARTICLE INFO

Handling Editor: Dr. Xavier Querol

Keywords:
COVID-19
Submicron aerosol
Source apportionment
Secondary formation

ABSTRACT

Restrictions on human activities were implemented in China to cope with the outbreak of the Coronavirus Disease 2019 (COVID-19), providing an opportunity to investigate the impacts of anthropogenic emissions on air quality. Intensive real-time measurements were made to compare primary emissions and secondary aerosol formation in Xi'an, China before and during the COVID-19 lockdown. Decreases in mass concentrations of particulate matter (PM) and its components were observed during the lockdown with reductions of 32–51%. The dominant contributor of PM was organic aerosol (OA), and results of a hybrid environmental receptor model indicated OA was composed of four primary OA (POA) factors (hydrocarbon-like OA (HOA), cooking OA (COA), biomass burning OA (BBOA), and coal combustion OA (CCOA)) and two oxygenated OA (OOA) factors (less-oxidized OOA (LO-OOA) and more-oxidized OOA (MO-OOA)). The mass concentrations of OA factors decreased from before to during the lockdown over a range of 17% to 58%, and they were affected by control measures and secondary processes. Correlations of secondary aerosols/ΔCO with O_x (NO_2 + O_3) and aerosol liquid water content indicated that photochemical oxidation had a greater effect on the formation of nitrate and two OOAs than sulfate; however, aqueous-phase reaction presented a more complex effect on secondary aerosols formation at different relative humidity condition. The formation efficiencies of secondary aerosols were enhanced during the lockdown as the increase of atmospheric oxidation capacity. Analyses of pollution episodes highlighted the importance of OA, especially the LO-OOA, for air pollution during the lockdown.

1. Introduction

With rapid economic growth and increases in energy consumption, China has suffered serious air pollution in recent decades (Zhang et al., 2015), especially high levels of aerosols in winter (Huang et al., 2014). The development of effective remedies for the air pollution problems will require a thorough understanding of the chemical composition, sources, and formation of aerosols. In the past, most air pollution studies in China relied on offline filter sampling (e.g., Cao et al., 2004; Gao et al., 2017; Wang et al., 2015; Zhang et al., 2013), but due to the low time-resolution of those methods (e.g., ~24 h), relatively limited information has been obtained on the temporal evolution of pollution events. To fill this gap, aerosol mass spectrometers with high-time resolution have been used more recently to monitor in real-time the non-refractory submicron aerosol (NR-PM_1) and the concentrations of its chemical constituents, including organic aerosol (OA), nitrate, sulfate, ammonium, and chloride (Hu et al., 2016; Sun et al., 2014; Wang et al., 2016; Wang et al., 2017). The OA can be resolved into primary OA (POA) and oxygenated OA (OOA) through the use of atmospheric receptor models (Canonaco et al., 2013). The POA can be further separated into hydrocarbon-like OA (HOA), cooking OA (COA), biomass burning OA (BBOA), and coal combustion OA (CCOA), while OOA includes less-oxidized OOA (LO-OOA) and more-oxidized OOA (MO-OOA) based on oxidation state (Kim et al., 2017; Lanz et al., 2007; Xu et al., 2017). The

* Corresponding authors at: Key Laboratory of Aerosol Chemistry and Physics, State Key Laboratory of Loess and Quaternary Geology, Institute of Earth Environment, Chinese Academy of Sciences, Xi'an 710061, China.
E-mail addresses: wangqy@ieecas.cn (Q. Wang), cao@loess.llqg.ac.cn (J. Cao).

https://doi.org/10.1016/j.envint.2021.106426
Received 2 August 2020; Received in revised form 24 January 2021; Accepted 26 January 2021
Available online 9 February 2021

real-time methods can provide insights into the chemical composition, sources, and formation processes of aerosols, and that information is useful for accurately assessing the environmental effects of aerosols and developing effective control measures.

A series of national active clean air policies targeting air pollution has been promulgated by the State Council of the People's Republic of China beginning in 2013; these include the Action Plan for the Prevention and Control of Air Pollution released on 2013 and the Three-year Plan on Defending the Blue Sky implemented in 2018. Previous studies have shown that China's clean air actions have led to some success in reducing pollutants (Feng et al., 2019; Ma et al., 2019; Zhang et al., 2019; Zheng et al., 2018). For example, Zheng et al. (2018) reported the following reductions in anthropogenic emissions in China from 2013 to 2017 due to the enactment of emission standards and stringent source controls: PM_{10} (36%), $PM_{2.5}$ (33%), organic carbon (OC) (32%), black carbon (BC) (28%), NO_x (21%), SO_2 (59%), and CO (23%). Although the clean air policies have led to significant reductions in air pollutants, additional actions and investigations are needed to further improve air quality.

In response to the abrupt outbreak of the Coronavirus Disease 2019 (COVID-19), numerous cities in China elevated the public health emergency response to level I, and strict restrictions were mandated by the Chinese State Council to curb the outbreaks. These measures included traffic restrictions, the closing non-essential industries, business, and schools, bans on public meetings, and suspension of construction activities, etc (http://www.gov.cn/yjgl/2006–02/26/content_211654.htm, in Chinese). The COVID-19 lockdown has made it possible to investigate the unprecedented restrictions of human activities on anthropogenic emissions and air pollution in China. To date, substantial reductions in aerosols and gaseous pollutants (e.g., NO_x and SO_2) have been reported for China during the COVID-19 lockdown (Li et al., 2020b; Wang et al., 2020c; Zhao et al., 2020; Zheng et al., 2020). However, other studies have shown unexpected high loadings of aerosol continued during the restrict period, and that has been attributed to limited effects in primary emissions under unfavorable meteorological conditions (Wang et al., 2020a) and the enhanced secondary aerosol formation (Le et al., 2020).

Indeed, current studies have shown large variations in air chemistry and quality improvements following the implementation of pollution control measures in different regions of China. For example, Le et al. (2020) and Huang et al. (2020) reported that both the oxidation capacity and production of secondary species were enhanced in eastern China during COVID-19 lockdown, and these offset the reductions in primary emissions. In contrast, Xu et al. (2020) found that the production rates for secondary inorganic and organic aerosols decrease in Lanzhou, a large city in western China, during the control period. Overall, the information on the variations in chemical composition, sources, and formation processes of aerosols in different cities in China during the COVID-19 lockdown has shown mixed effects on air quality, and the consequences of the restrictions are just beginning to be understood.

The Fenwei Plain is designated as the key pollution control region in China since 2018. As one of megacities in this plain, Xi'an (34°16′ N, 108°54′ E) has been facing severe air pollution problem, especially in winter (Niu et al., 2016; Wang et al., 2015). For example, over 75% of days were polluted in Xi'an during winter 2018, including three days of severe pollution (air quality index (AQI) > 300), twenty-two days of heavy pollution (201 < AQI < 300), thirteen days of medium pollution (151 < AQI < 200), and thirty days of light pollution (101 < AQI < 150) (http://sthjt.shaanxi.gov.cn). The COVID-19 lockdown provided a unique opportunity to assess the influence of anthropogenic activities on air quality in Xi'an. For the present study, real-time measurements of both aerosols and gaseous pollutants were conducted to investigate the impacts of changes in primary emissions and the importance of secondary aerosol formation in Xi'an. The main objectives of this study were to (1) investigate the changes in the loadings and composition of aerosols during the COVID-19 lockdown; (2) determine the sources for assessing control measures and formation processes of secondary OA; and (3) explore the cause of air pollution during the COVID-19 lockdown. The comparisons and contrasts before versus during the COVID-19 lockdown shed insights into the complexities of aerosol chemistry and air pollution under strict restrictions on normal activities. The results of the study also will provide scientific guidance for developing aerosol pollution control strategies for the Fenwei Plain.

2. Methodology

2.1. Research site and period

Intensive online measurements were performed from 1 January to 9 February 2020 at the rooftop of an office building (~10 m above ground level, 34°13′ N, 108°52′ E) in the southwest of downtown Xi'an (Supplementary Material Fig. S1). The sampling site has been served as a typical urban observation place (e.g., Wang et al., 2015; Zhang et al., 2014), which is surrounded by residential and commercial areas without intense industrial activities or local fugitive dust sources nearby. Based on the implementation date of the public health emergency response I in Xi'an city, the study period was broken down into two stages: (1) the normal period from 1 to 25 January and (2) the COVID-19 lockdown period from 26 January to 9 February. The latter 15 days were considered representative of the lockdown period during the strictest restrictions on activities in the city.

2.2. Online measurements

2.2.1. Aerosol chemical speciation monitor

A quadrupole aerosol chemical speciation monitor (ACSM, Aerodyne Research Inc., Billerica, Massachusetts, USA) was used to measure the non-refractory submicron aerosol (NR-PM_1), including OA, nitrate, sulfate, ammonium, and chloride, at a time resolution of 15-min. A detailed description of the operational principles and calibration method for the ACSM can be found in Ng et al. (2011c). Briefly, the vacuum chamber of the instrument includes a particle aerodynamic lens, a thermal particle vaporizer, and a mass spectrometer. For our study, the sampled ambient air stream passed through a $PM_{2.5}$ impactor inlet and a Nafion® dryer (MD-700-24S-1; Perma Pure, Inc., Lakewood, NJ, USA) at a flowrate of 3 L min^{-1} before entering the ACSM. The aerodynamic lens coupled with a 100 μm diameter critical aperture created a beam of focused submicron particles (~40–1000 nm aerodynamic diameter) at a flowrate of ~0.1 L min^{-1}. The focused particle beam was heated by a thermal particle vaporizer, which operated at 600 °C, and the vaporized species were then ionized by 70 eV electron ionization and subsequently characterized by the quadrupole mass spectrometer.

Before sampling, ammonium nitrate (NH_4NO_3) aerosol was used for calibration and to ensure the accuracy of the instrument. The NH_4NO_3 particles were generated with the use of an atomizer (Model 9302, TSI Inc., Shoreview, MN, USA) and a prepared NH_4NO_3 solution. Then, a differential mobility analyzer (DMA, TSI model 3080, TSI Inc., Shoreview, MN, USA) was used to select the particle size, and a condensation particle counter (CPC, TSI model 3772, TSI Inc., Shoreview, MN, USA) was used to determine particle number. The response factors (RFs) for nitrate and ammonium were obtained by fitting the measured ion signals (in amps) recorded by the ACSM against the calculated mass concentrations (in μg m^{-3}) from the combined DMA and CPC data (Fig. S2). The relative ionization efficiency (RIE) for ammonium was directly calculated as the ratio of the RFs for ammonium and nitrate.

The ACSM local tool version 1.5.3.5 (Aerodyne Research Inc., Billerica, Massachusetts, USA) compiled with Igor Pro 6.37 (Wavemetrics, Lake Oswego, OR) was used to analyse the measured ACSM standard data. The RIEs for OA, nitrate, and chloride were set to 1.4, 1.1, and 1.3 by default, respectively. The RIE for ammonium (5.8) was determined from the NH_4NO_3 calibration, while the RIE for sulfate (1.9) was estimated by fitting the measured sulfate versus predicted sulfate values

following the method suggested by Budisulistiorini et al. (2014) (Text S1). With the default collection efficiency (CE) value (1), the ammonium concentration obtained was adequate for particle neutralization (Fig. S3) and the average mass fraction of ammonium nitrate in NR-PM_1 (0.37) was < 0.4. As the sampled air was dried before entering the ACSM, the impacts of high levels of aerosol acidity, ammonium nitrate fraction, and relative humidity for CE were expected to be negligible (Middlebrook et al., 2012). Therefore, a constant CE of 0.45 was used in this study. The concentration and error matrices of mass-to-charge (*m/z*) fragments from 12 to 120 derived from OA data were initialized by the method of Allan et al. (2003). Following the protocol described by Ulbrich et al. (2009), the error values of *m/z* 44 were multiplied by 2 to account for the contributions from gas-phase carbon dioxide. Other *m/z* fragments with high signal-to-noise (SNR > 2) were not specially treated. In addition, *m/z* 12 was removed from all ACSM data prior to source apportionment owing to numerous negative values. After these adjustments, 92 fragments were finally used as receptor model inputs.

2.2.2. Aethalometer measurement

An aethalometer (model AE33, Magee Scientific, Berkeley, CA, USA) equipped with a $PM_{2.5}$ cyclone particle separator on the inlet was used to measure BC mass concentrations ($BC_{2.5}$) at a time resolution of 1-min. The model AE33 uses a real-time, loading effect, compensation algorithm based on two parallel spot measurements of optical absorption to eliminate the nonlinear loading effect (Drinovec et al., 2015). The light attenuation transmitted through two spots with different sample flows was obtained at seven wavelengths (λ = 370, 470, 525, 590, 660, 880, and 940 nm). The light attenuation at λ = 880 nm was used to calculate the BC loadings due to the negligible contributions from other light-absorbing components, especially brown carbon and mineral dust (Kirchstetter and Thatcher, 2012). A detailed description of the AE33 aethalometer can be found in Drinovec et al. (2015).

2.2.3. Complementary instruments

The concentrations of NO_x (NO + NO_2), SO_2, CO, and O_3 were measured with the use of a nitrogen oxides analyzer (EC9841, Ecotech Pty Ltd, Australia), a sulfur dioxide analyzer (EC9850, Ecotech Pty Ltd, Australia), a carbon monoxide analyzer (Thermo 48i, Thermo Scientific Inc., Franklin, MA, USA), and an ozone analyzer (EC9810, Ecotech Pty Ltd, Australia), respectively. Meteorological parameters, including wind speed (WS), wind direction (WD), relative humidity (RH), and temperature (T), were measured using an integrated automatic weather station (MAWS201, Vaisala, Helsinki, Finland). The planetary boundary layer height (PBLH) was obtained using the gridded data from Global Data Assimilation System (GDAS) (ftp://arlftp.arlhq.noaa.gov/pub/archives/gdas1).

2.3. Source apportionment analysis

2.3.1. Hybrid environmental receptor model

The hybrid environmental receptor model (HERM) developed by Institute of Earth Environment, Chinese Academy of Sciences and University of Nevada, Las Vegas is a new technical approach for source apportionment of particulate and gaseous pollutants (Chen and Cao, 2018). Similar to other receptor models, such as positive matrix factorization (PMF) and multilinear engine (ME-2) (Paatero and Tapper, 1994; Canonaco et al., 2013), the HERM groups air pollutants measured at a receptor site into the emissions of individual sources using information on their chemical compositions. Here, the HERM was used only to apportion the OA sources. To solve the mass balance of OA, the bilinear HERM in matrix notation was defined as:

$$C_{ik} = \sum_{j=1}^{J} F_{ij} S_{jk} + E_{ik} \quad (1)$$

where C_{ik} is the measured concentration of *m/z i* during time *k*; F_{ij} is the source profile, that is, the fractional quantity of *m/z i* in source *j* emission; S_{jk} represents the contribution of source *j* during time *k*; and E_{ik} is the model residual for *m/z i* concentration measured during time *k*.

Based on the modified ME-2 Basic_2way script, the HERM was developed as a bridge between CMB and PMF by allowing the use of a partial F_{ij} matrix of source profiles. When the matrix of F_{ij} is fully known and constrained, the HERM reverts to a CMB model for evaluating the contribution of source (S_{jk}) only. Compared with the CMB software (i.e., EPA CMB v8.2), the current HERM version 1.8 software has advantages of the ability to analyze multiple samples in a single run, non-negativity constraints, and better tolerance of collinearity. When the F_{ij} and S_{jk} matrices are fully unknown, the HERM is converted to a PMF model, and the solution F_{ij} and S_{jk} with non-negativity constraints are not unique due to rotational ambiguity. To solve the problem of incomplete source profiles of emission sources when using CMB, and to reduce the rotational degrees of freedom in PMF, the HERM allows a hybrid model that constrains a partial F_{ij} by inputting one or more source profiles (row of F). Naturally, more reliable source profile information can lead to better separations of mixed sources.

The HERM accounts for uncertainties in both C_{ik} ($\sigma_{C_{ik}}$) and constrained F_{ij} ($\sigma_{F_{ij}}$), which are related to errors in the ambient measurements and variability in source emissions, respectively. Based on an iterative conjugate gradient algorithm, the HERM solves S_{jk} and unknown F_{ij} by minimizing the reduced chi-square (Q):

$$Q = \sum_{k=1}^{K} \sum_{i=1}^{I} \frac{\left(C_{ik} - \sum_{j=1}^{J} F_{ij} S_{jk}\right)^2}{\sigma_{C_{ik}}^2 + \sum_{j=1}^{J} \left(\sigma_{F_{ij}}^2 \sigma_{S_{jk}}^2 + \beta \delta_{ij} \sigma_{C_{ik}}^2\right)} \quad (2)$$

in which K, I, and J represent the number of times, *m/z* fragments, and sources, respectively; δ_{ij} is set to 0 or 1 depending on whether F_{ij} is constrained or unknown, respectively; and β is an adjustable factor with a default value of 1. For the HERM, the expected Q (Q_{exp}) equals the degree of freedom of the model solution $(I \times J - K \times (I + J) + C)$, where C is the number of constrained source profiles.

2.3.2. Optimized source apportionment of OA

The HERM (software version 1.8) was applied to analyze the OA dataset. As there is no specific source profile available for fireworks, the data related to Spring Festival Eve and the first two days (24 to 26 January) and the Lantern Festival (8 to 9 February) were excluded in OA source apportionment. In the first step of the procedure, a range of two to eight factor was explored for the OA data using the PMF model with completely unconstrained source profile because the extracted factors could be associated with distinct sources (Fröhlich et al., 2015). Diagnostic plots for PMF solution are detailed and documented in the supplementary material (Text S2 and Fig. S4–S9).

The PMF model analysis showed that six factor solution, which included HOA, COA, BBOA, CCOA, LO-OOA, and MO-OOA, was most interpretable. However, in the 6-factor unconstrained PMF model solution, BBOA was not split, but rather mixed with OOA. For the investigations of other PMF solutions (5, 7, and 8 factors), sufficient separations of the clean BBOA factor were achieved through contributions at *m/z* 60 (2.2–3.2%), *m/z* 73 (1.6–2.5%), and *m/z* 44 (2.3–3.2%) in the profile and good correlations (R^2 = 0.91–0.96) between *m/z* 60 and *m/z* 73 and the BBOA factor. Individual BBOA profiles obtained in the 5-, 7-, and 8-factor PMF solutions showed great similarities (uncentered correlation coefficients (UC) = 0.98–0.99) (Ulbrich et al., 2009). Therefore, the mean of the clearly-resolved BBOA profiles was extracted and used as the anchor profile in subsequent 6-factor HERM analysis to separate the BBOA from OOA. Here, the standard deviation of the BBOA profiles for different factor solutions was also input into the HERM as they reflected the uncertainties in constrained source profile. Finally, six factors, identified as HOA, COA, BBOA, CCOA, LO-OOA, and MO-OOA, in the optimal HERM solution matched the criteria of distinct source profiles and time series, typical diurnal patterns, and strong

correlations with external tracers of sources. A detailed description of the final adopted profiles and time series of resolved OA factors can be found in Section 3.2.

2.4. Aerosol liquid water content

The aerosol liquid water content (ALWC) was calculated using the ISORROPIA-II thermodynamic equilibrium model (http://isorropia.eas.gatech.edu). The mass concentrations of NR-PM_1 species (nitrate, sulfate, ammonium, and chloride) and meteorological parameters (RH and T) were input into the model to retrieve the ALWC concentrations. Details of the model can be found in Fountoukis and Nenes. (2007).

2.5. Air quality index

The air quality index (AQI) is a parameter that used to describe the degree of air pollution in China, and it is calculated from the concentrations of six priority pollutants (i.e., PM_{10}, $PM_{2.5}$, SO_2, NO_2, CO, and O_3) (Zheng et al., 2014). According to the Technical Regulation on Ambient Air Quality Index formulated by the Chinese Ministry of Environmental Protection (MEE, 2012), the air quality is classified as excellent (0 < AQI < 50), good (51 < AQI < 100), light pollution (101 < AQI < 150), medium pollution (151 < AQI < 200), heavy pollution (201 < AQI < 300), and severe pollution (300 < AQI). Real-time AQIs in Xi'an were obtained from the Department of Ecology and Environment of Shaanxi Province (http://sthjt.shaanxi.gov.cn).

2.6. Nitrogen and sulfur oxidation ratio

The nitrogen oxidation ratio (NOR) and sulfur oxidation ratio (SOR) were calculated to evaluate the degree of secondary conversion of gas precursors NO_2 and SO_2 (Yang et al., 2017; Zhang et al., 2011):

$$NOR = \frac{n(nitrate)}{n(nitrate) + n(NO_2)} \quad (3)$$

$$SOR = \frac{n(sulfate)}{n(sulfate) + n(SO_2)} \quad (4)$$

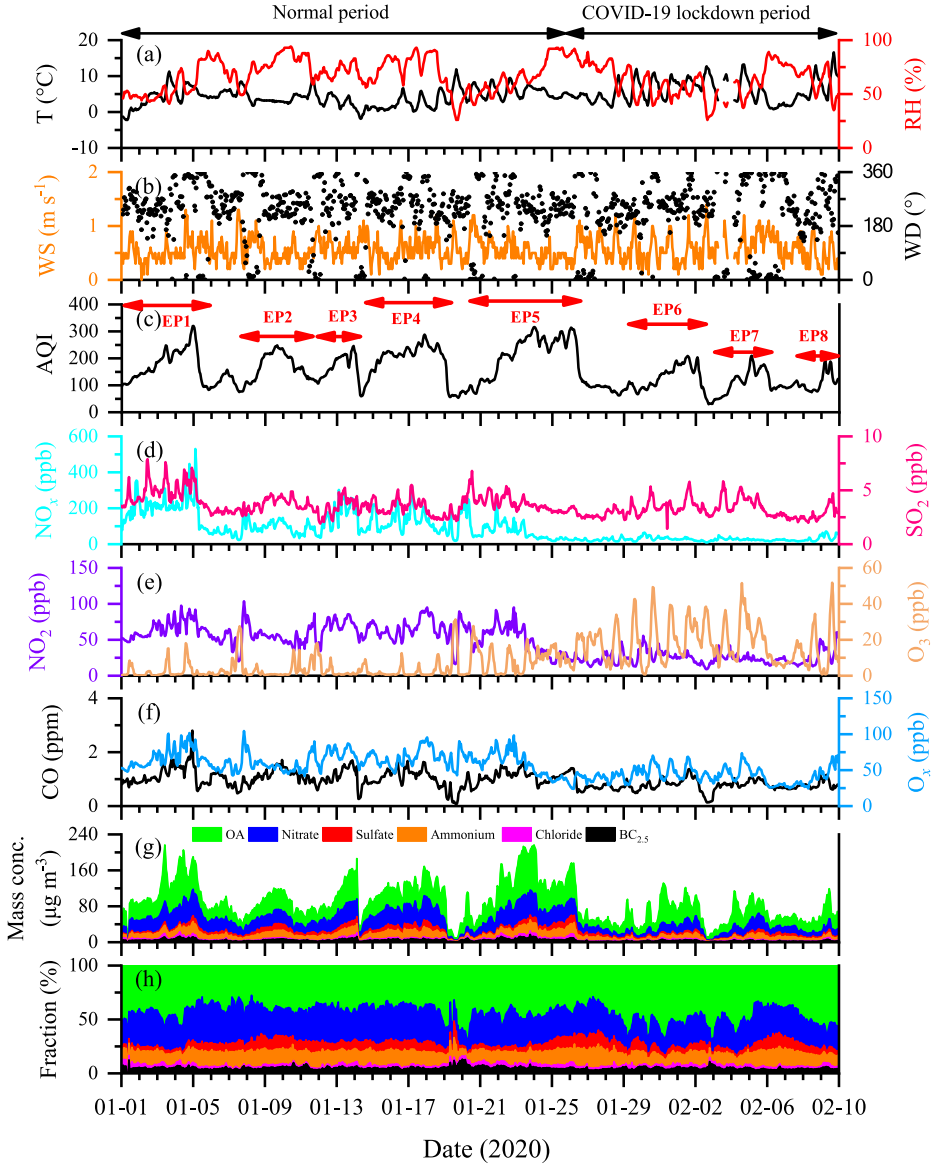

Fig. 1. Time series of (a) temperature (T), relative humidity (RH), (b) wind speed (WS), wind direction (WD), (c) Air Quality Index (AQI), (d) NO_x, SO_2, (e) NO_2, O_3, (f) CO, O_x, (g–h) mass concentration and fraction of chemical species in PM in Xi'an from 1 January to 9 February 2020. Polluted episodes (EPs) were defined as days when AQI > 100.

where n(nitrate), n(NO_2), n(sulfate), and n(SO_2) are the molar concentrations of nitrate, NO_2, sulfate, and SO_2, respectively.

3. Results and discussion

3.1. Overview of PM characteristics

Fig. 1 shows the temporal variations in mass concentrations of particulate matter (PM = OA + nitrate + sulfate + ammonium + chloride + $BC_{2.5}$) and selected species, mixing ratios of gaseous pollutants, and meteorological conditions during the campaign period. Summary statistics for the normal (1 to 23 January) and COVID-19 lockdown (27 January to 7 February) periods are summarized in Table 1. The average PM concentration was 60.2 ± 26.1 μg m^{-3} during the COVID-19 lockdown period, which was 41% lower than that recorded during the normal period (102.0 ± 42.7 μg m^{-3}). Large reduction rates in PM_1 were also found for several strict short-term pollution control events, such as 2008 Beijing Olympic Games (46%) (Huang et al., 2010), 2014 Asia-Pacific Economic Cooperation summit (53–63%) (Han et al., 2015; Xu et al., 2015; Zhang et al., 2016), and 2015 China Victory Day (57%) (Zhao et al., 2017). These results demonstrate that the controls implemented during the COVID-19 lockdown in Xi'an did have beneficial effects on air quality, but even though the PM loading decreased notably, it was higher than the China National Ambient Air Quality Grade I Standard of 35 μg m^{-3} for annual $PM_{2.5}$ (GB3095-2012), indicating the air pollution episodes occurred.

Compared with the normal period, obvious decreases in PM components were observed during the COVID-19 lockdown period with reductions ranging from 32% to 51% (Table 1). The largest difference was for nitrate, which can be explained by large reductions of its NO_x precursors; in fact, the NO_x concentrations decreased by 80% during the lockdown (Table 1), almost certainly due to the controls on motor vehicles. The composition of PM was generally similar for the two periods, which was mainly composed of OA, followed by nitrate, ammonium, sulfate, $BC_{2.5}$, and chloride (Fig. 2a and b). However, the average contribution of OA to PM was higher and that of nitrate was smaller during the COVID-19 lockdown compared with the prior conditions. To better understand the impact of chemical species on PM, the mass fractions of each species were plotted as a function of PM mass concentrations during the two different periods (Fig. 2c and d). The PM mass concentration showed a bimodal distribution during the normal period but a unimodal distribution during the COVID-19 lockdown period. Moreover, the mass fractions of each chemical species kept relative stable at the PM range of 40–170 μg m^{-3} during the normal period, and OA contributed the most to PM mass (42 ± 2%). In the COVID-19 lockdown, the mass fraction of OA showed an obvious increasing trend from 42% when PM was in the range of 40–60 μg m^{-3} to 60% when PM was > 110 μg m^{-3}. In contrast, the mass fractions of secondary inorganic aerosols showed decreasing trends as the PM mass increased. These results highlighted the important contribution of OA to air pollution during the COVID-19 lockdown period.

Table 1
Summary of meteorological parameters, mixing ratios of gaseous pollutants, mass concentrations of PM species and OA components during the normal and COVID-19 lockdown periods.

	Grand average	Normal period[a]	COVID-19 lockdown period[b]	Change ratio[c]
Meteorological parameters				
T (°C)	4.6 ± 2.9	4.1 ± 2.5	5.8 ± 3.2	−42%
RH (%)	64.9 ± 15.2	66.6 ± 15.2	61.4 ± 14.7	8%
WS (m s^{-1})	0.58 ± 0.23	0.56 ± 0.22	0.60 ± 0.25	−6%
Gaseous pollutants (ppb)				
NO_x	94.1 ± 78.2	129.4 ± 75.0	26.4 ± 9.3	80%
SO_2	3.7 ± 1.0	3.9 ± 1.0	3.3 ± 0.8	14%
NO_2	48.7 ± 21.8	61.5 ± 14.7	24.2 ± 7.9	61%
O_3	9.0 ± 10.7	4.0 ± 5.9	18.6 ± 11.2	−364%
CO (ppm)	1.0 ± 0.3	1.1 ± 0.3	0.8 ± 0.2	29%
O_x	57.7 ± 16.3	65.5 ± 12.8	42.8 ± 10.9	35%
PM species (μg m^{-3})				
PM	87.7 ± 42.9	102.0 ± 42.7	60.2 ± 26.1	41%
OA	38.6 ± 20.9	43.3 ± 21.3	29.4 ± 16.5	32%
HOA	5.5 ± 4.6	6.8 ± 4.9	2.8 ± 2.5	58%
COA	4.5 ± 2.5	4.8 ± 2.7	4.0 ± 2.1	17%
BBOA	4.7 ± 4.0	5.1 ± 4.3	4.0 ± 3.4	21%
CCOA	3.7 ± 2.9	4.2 ± 2.9	2.6 ± 2.6	38%
LO-OOA	7.5 ± 5.8	8.6 ± 6.4	5.6 ± 3.7	35%
MO-OOA	11.1 ± 4.5	12.0 ± 4.9	9.5 ± 3.3	21%
Nitrate	25.6 ± 13.5	31.0 ± 12.8	15.1 ± 6.8	51%
Sulfate	6.0 ± 3.3	6.9 ± 3.6	4.3 ± 1.9	37%
Ammonium	10.8 ± 5.2	12.7 ± 5.1	7.2 ± 3.0	43%
Chloride	2.3 ± 1.6	2.7 ± 1.8	1.5 ± 0.8	44%
$BC_{2.5}$	4.4 ± 2.6	5.3 ± 2.6	2.7 ± 1.3	50%

[a] The normal period was from 1 to 23 January 2020.
[b] The COVID-19 lockdown period was from 27 January to 7 February 2020.
[c] Change ratio = ([Normal period] - [COVID-19 lockdown period])/[Normal period].

Fig. S10 shows the diurnal variations of each measured PM species during the normal and COVID-19 lockdown periods. Nitrate displayed a similar diurnal pattern for the two periods (Fig. S10a). That is, the nitrate mass concentration started to increase after sunrise (~07:00–08:00) and reached its peak value around noon, which can be attributed to increased photochemical oxidation during the day as discussed in Section 3.3. Later, owing to more favourable diffusion conditions, especially increased PBLHs and higher WSs (Fig. S11c and d), nitrate gradually decreased in the afternoon. After sunset, nitrate increased again. It was probably at least partly a result of higher RH (Fig. S11b), which would promote nitrate formation through the aqueous-phase reactions (see discussion in Section 3.3). Meanwhile, the low nocturnal PBLHs and WSs at night can further aggravated the nitrate accumulation. In contrast to nitrate, the diurnal variation of sulfate showed distinctly different trends during the normal versus COVID-19 lockdown periods (Fig. S10b). Both nitrate and sulfate loadings increased after sunrise, but for sulfate, this can best be explained by the downward mixing of sulphate particles that formed at night in a residual layer aloft. In the afternoon, sulfate continued to increase during the normal period but obviously decreased during the lockdown period. Although the high PBLHs and WSs in the afternoon favoured pollutant dispersal and dilution, the increases in sulfate during the normal period were likely a result of regional transport because pollutants typically accumulated in the Guanzhong Basin (Fig. S1b) during winter (Niu et al., 2016). The enhanced sulfate at night during both periods can be explained by a combination of the low PBLHs and the enhanced formation through aqueous-phase reaction under high RHs (Sun et al., 2013). As ammonium can be neutralized by nitrate, sulfate, and chloride (Fig. S12), the diurnal pattern of this substance presumably was driven by the variations of these other species (Fig. S10c). The diurnal profile of OA was similar during the normal and COVID-19 lockdown periods, which was characterized by increases at night, relatively stable concentrations in the morning, and decreases in the afternoon. This pattern was associated with daily variations in meteorological condition as well as primary emissions and secondary aerosol formation, as discussed in Section 3.2. Owing to the combined influences of PBLH, WS, and combustion emissions, the diurnal patterns in $BC_{2.5}$ and chloride showed similar trends with clear increases at night and decreases in the afternoon during both the normal and lockdown periods.

3.2. OA composition, sources, and variations

Six OA factors were resolved by the HERM, including four POA factors (HOA, COA, BBOA, and CCOA) and two OOA factors (LO-OOA and MO-OOA). The profiles and temporal variations and the contributions to the total OA mass for six OA factors are shown in Fig. 3 and Fig. 4, respectively. Detailed characteristics of specific OA factors during

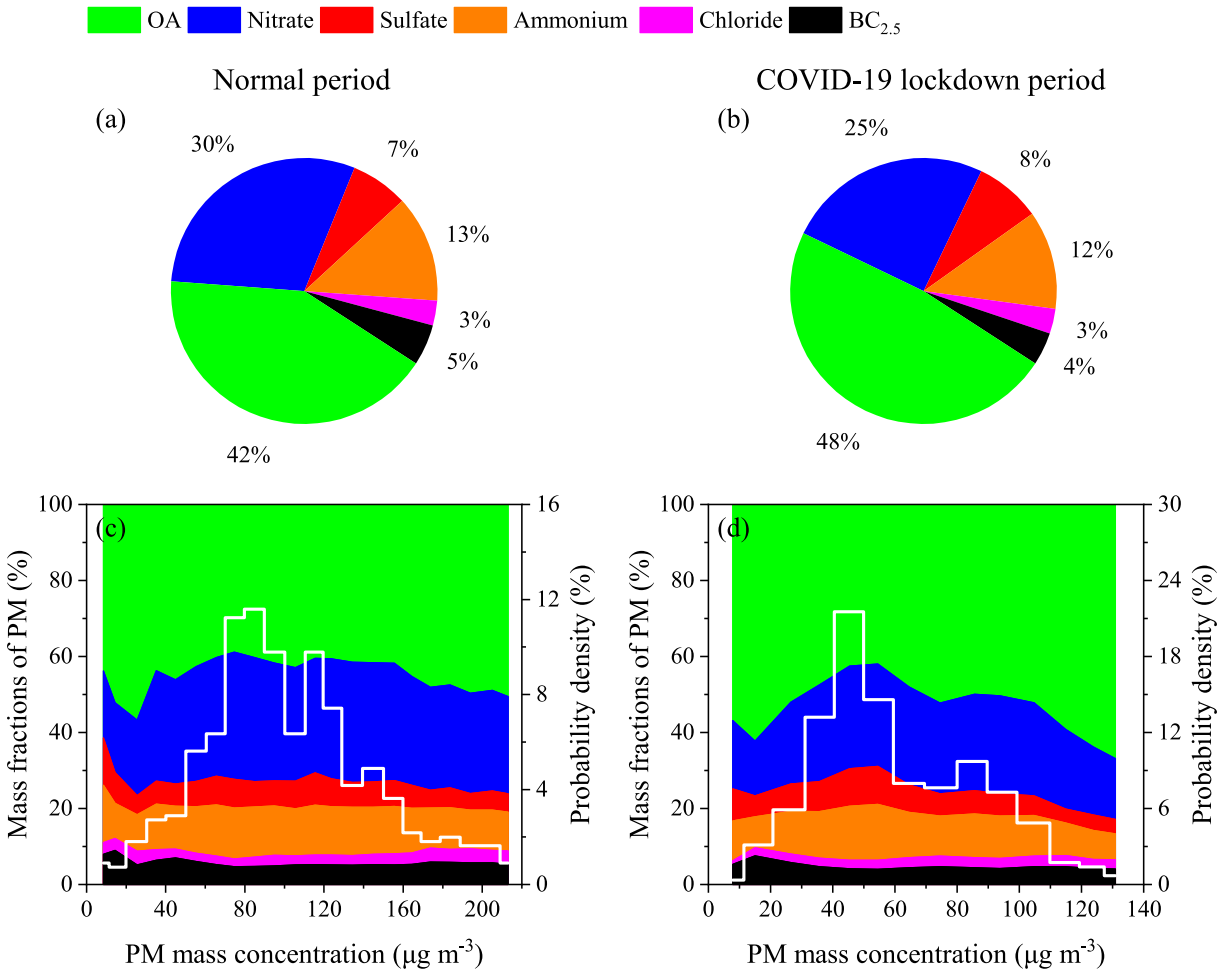

Fig. 2. Averaged contributions of PM species to the total PM mass during the (a) normal and (b) COVID-19 lockdown periods. Variation of the percent composition with the PM concentration during the (c) normal and (d) COVID-19 lockdown periods were also shown. The white solid lines show the probability densities for the PM mass.

the normal and COVID-19 lockdown periods are discussed below.

3.2.1. *Hydrocarbon-like OA (HOA)*

As shown in Fig. 3a, the HOA profile was primarily characterized by alkyl fragments ($C_nH^+_{2n+1}$ and $C_nH^+_{2n-1}$), and it had major peaks at *m/z* 41 (7.3%), 43 (6.3%), 55 (7.1%), and 57 (5.1%). The temporal variations of HOA correlated more strongly with NO_x ($R^2 = 0.45$) compared with the other POAs (R^2 = 0.02–0.21), supporting an association of HOA with motor vehicle emissions. Similar results also have been reported for other urban sites in China (Li et al., 2017; Sun et al., 2016; Wang et al., 2020b).

During the normal period, the mass concentration of HOA was 6.8 ± 4.9 μg m^{-3}, accounting for 16% of the total OA mass (Fig. 4a). Its diurnal pattern presented an increase around 07:00–09:00, which can be explained by the emissions from morning rush-hour traffic (Fig. S13a), and this was consistent with the high NO_x during this period (Fig. S14). Later in the day, decreases in HOA were associated with reduced traffic coupled with higher PBLHs and stronger WSs that led to particle dilution and dispersion (Fig. S11). An increase in HOA mass concentrations starting at ~17:00 paralleled an increasing trend of NO_x, which was mainly related to the evening rush-hour traffic. Due to the low nocturnal PBLHs and relative stable winds, HOA accumulated gradually until ~21:00 when fewer and fewer vehicles were on the roads (Liu et al., 2018). However, in the present study HOA rose at 01:00–04:00, which was likely related to the emissions from diesel trucks and heavy-duty vehicles that were banned during the day. The high NO_x at 03:00–04:00 is also compelling evidence for impacts from traffic emissions. For comparison, all private cars and diesel trucks used for construction activities were restricted during the COVID-19 lockdown when the average HOA mass concentration decreased to 2.8 ± 2.5 μg m^{-3} (9% of OA) (Fig. 4b). This reduction in HOA (58%) was the largest of the six OA factors, indicating that the impacts of the lockdown on transportation had a large effect on pollutant emissions (Wang et al., 2020c). The morning and nighttime traffic-related HOA peaks that occurred during the normal period were not seen during the COVID-19 lockdown (Figure S13a). The increasing trend of HOA after midnight during the COVID-19 lockdown is best explained by the accumulation of locally generated HOA under stable meteorological conditions.

3.2.2. *Cooking OA (COA)*

The COA profile adopted in this study was characterized by prominent alkyl fragment peaks of *m/z* 41 (11.1%), 43 (8.4%), 55 (7.2%), and 57 (3.4%). Previous studies have shown that the heating of seed oils and animal fats leads to strong signals at *m/z* 41 and *m/z* 55 (Allan et al., 2010), and therefore, high *m/z* 41/43 and 55/57 ratios can be considered as key features for distinguishing the COA from other POAs (He et al., 2010; Mohr et al., 2012; Reyes-Villegas et al., 2018). Here the ratios *m/z* 41/43 (1.3) and *m/z* 55/57 (2.1) in the COA profile were higher than those in HOA (1.1 and 1.4), BBOA (0.1 and 1.6), and CCOA (0.7 and 1.0) profiles. Furthermore, the *m/z* 98 is used as a tracer for COA (Crippa et al., 2013b; Sun et al., 2011), and a good correlation was found between COA and *m/z* 98 in this study ($R^2 = 0.55$, Fig. 3b).

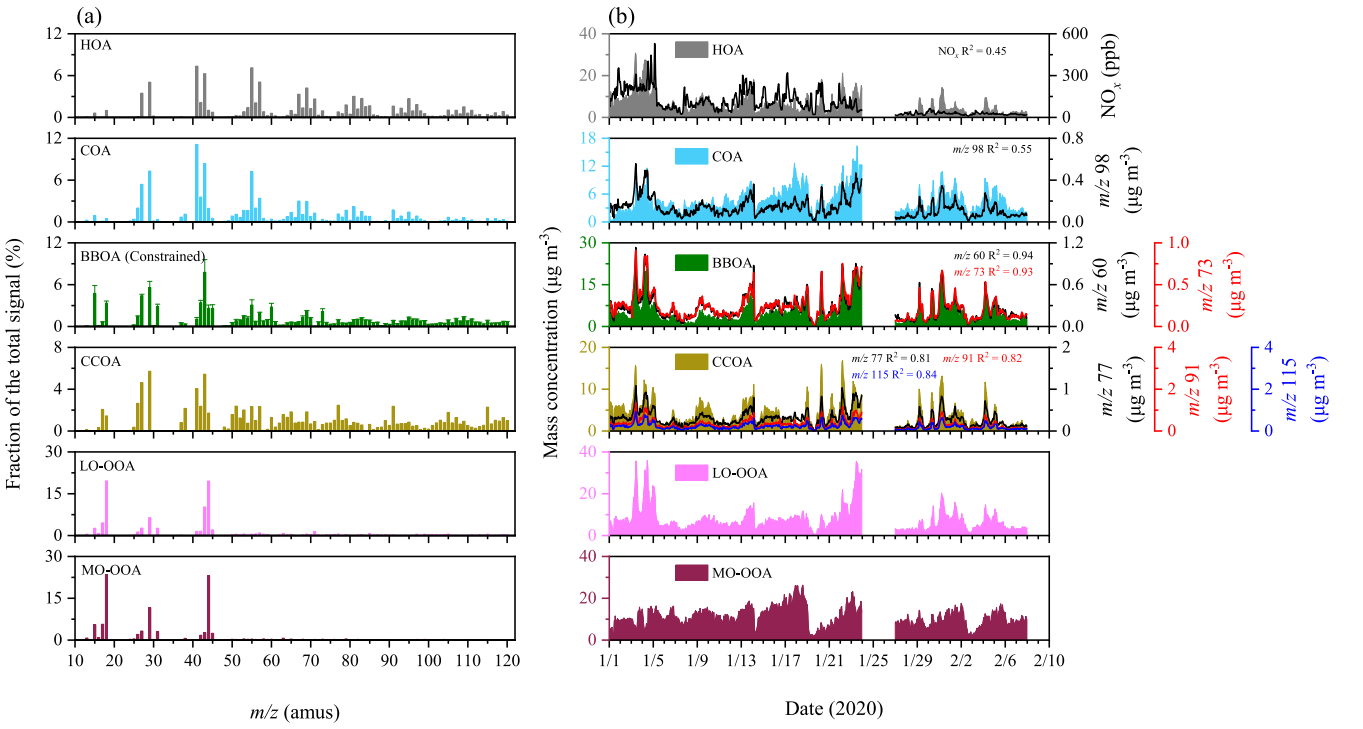

Fig. 3. (a) Profiles and (b) time series plots of six resolved OA factors, including HOA, COA, BBOA, CCOA, LO-OOA, and MO-OOA. The error bars for the BBOA profile represent the standard deviations from the 5-, 7-, and 8-factor PMF model solutions. The corresponding time trends of tracer compounds are also shown.

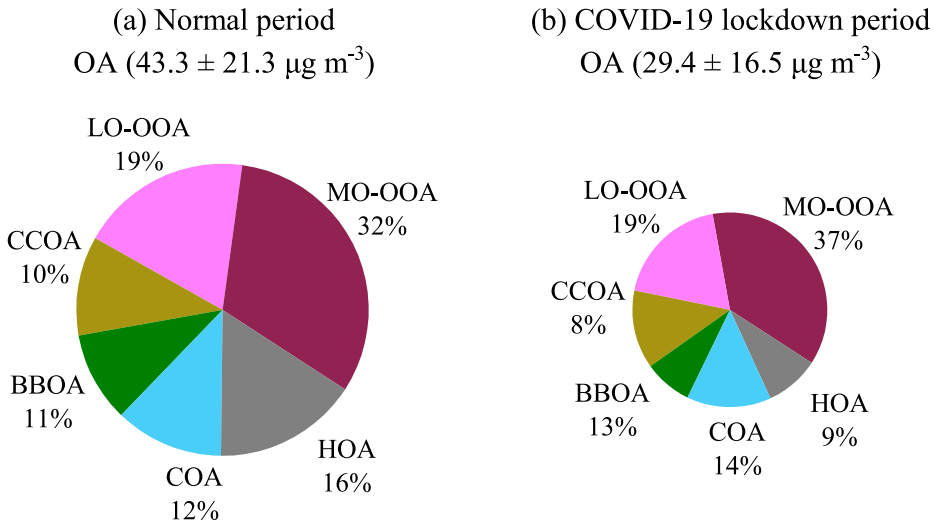

Fig. 4. Pie charts depicting the average fractional contributions of HOA, COA, BBOA, CCOA, LO-OOA, and MO-OOA to the total OA during the (a) normal and (b) COVID-19 lockdown periods. The areas of the two pies are scaled to be proportional to the mass concentrations of the total OA.

As shown in Fig. S13b, the diurnal cycle of COA during the normal period was characterized by obvious peaks at noon (12:00) and in the evening (20:00), which are the times when local catering establishments prepare lunches and dinners. These features in turn support the identification of this factor as COA. Due to the restrictions imposed on the catering during the COVID-19 lockdown period, these two peaks were then disappeared. Instead, the diurnal variations of COA showed a peak at 11:00, which around when residential cooking typically began, while the peak at 4:00 was probably associated with the accumulation of locally generated pollutants under stable meteorological condition at night. The average concentration of COA decreased from 4.8 ± 2.7 μg m^{-3} during the normal period to 4.0 ± 2.1 μg m^{-3} during the COVID-19 lockdown period, but the contribution of COA to OA increased from 12% to 14% (Fig. 4). Despite the closure of catering industries, people obviously still needed to cook during the COVID-19 lockdown, and this can explain the smallest reduction of COA (17%) among all of the OA factors during the lockdown.

3.2.3. *Biomass burning OA (BBOA)*

The constrained BBOA profile was featured by strong signals at *m/z* 60 (2.8%) and *m/z* 73 (2.2%) (Fig. 3a), which are typical molecular fragments of levoglucosan and related species (e.g., galactosan and mannosan) (Cubison et al., 2011). Furthermore, the temporal variations in BBOA correlated strongly with the fragment ions *m/z* 60 ($R^2 = 0.94$) and *m/z* 73 ($R^2 = 0.93$) (Fig. 3b). Indeed ~45% and 40% of the mass of *m/z* 60 and *m/z* 73 fragments can be explained by BBOA, respectively.

Additionally, the resolved BBOA profile showed strong similarities with biomass burning profiles obtained in previous studies (UC = 0.85–0.91) (Crippa et al., 2013a; Ng et al., 2011b), further supporting the identification of the BBOA factor in this study.

As shown in Fig. S13c, BBOA showed roughly similar diurnal patterns for the two different periods. The low values in the afternoon were attributed to the high PBLHs and strong WSs that promoted dispersion while the enhanced BBOA mass concentrations at night can be explained by the combined effects of domestic heating by biomass burning and the low nocturnal PBLHs. The mass concentration of BBOA decreased from 5.1 ± 4.3 μg m^{-3} during the normal period to 4.0 ± 3.4 μg m^{-3} during the lockdown period, equivalent to a reduction of 21%. It is noteworthy that the control measures did not include prohibitions on residential use of biofuels for heating and cooking. As all of our sampling in Xi'an was conducted during the heating season, the variations in heating demand probably had little effect on BBOA or CCOA (as discussed below). However, people were required to stay at home during the lockdown, and that likely reduced the amount of biomass burned in agricultural fields, which is a possible explanation for the decline in BBOA concentrations. Compared with other primary emissions, such as those from motor vehicles or industries, biomass burning is often sporadic and unorganized, thus tends to be more variable over time. Indeed, the effects of the lockdown on the biomass burning emissions were less than those of other sources, and the BBOA contribution to OA increased from 11% to 13% (Fig. 4) under the restrictions put in place during the lockdown. Therefore, the control of pollutants from biomass burning will be a key step for improving the air quality in Xi'an during the winter.

3.2.4. Coal combustion OA (CCOA)

The CCOA profile was dominated by the presence of alkyl fragments, especially a larger fraction of *m/z* 80–120 (32%) (Fig. 3a), and this shows that coal combustion OA contained relatively large proportions of high molecular-weight organic compounds. In particular, the PAH-related fragments (*m/z* 77, 91, and 115) had larger peaks (2.3–2.5%) in CCOA profile compared with other POAs, and strong correlations were observed between CCOA and these fragments (R^2 = 0.81 for *m/z* 77, R^2 = 0.82 for *m/z* 91, and R^2 = 0.84 for *m/z* 115) (Fig. 3b), consistent with previous studies (Lin et al., 2017; Zhou et al., 2016). As shown in Table 1, the mass concentration of CCOA decreased from 4.2 ± 2.9 μg m^{-3} (10% of OA) during the normal period to 2.6 ± 2.6 μg m^{-3} (8% of OA) during the lockdown period. The 38% reduction can be attributed to impacts of the lockdown on industries that use coal as their main energy source. Similar to BBOA, the diurnal variations of CCOA during the normal and COVID-19 lockdown periods presented high loadings at night and low values in the afternoon (Fig. S13d). The patterns can best be explained by the combustion of coal for residential heating and the daily cycle in the PBLH, and these results highlight the pervasive impacts of domestic coal combustion on air quality in Xi'an during winter.

3.2.5. Less and more-oxidized oxygenated OA (LO-OOA and MO-OOA)

Fig. 3a shows that both LO-OOA and MO-OOA had somewhat similar profile features, both having an abundant peak at *m/z* 44, which is an indicator of oxidized organic compounds (Ng et al., 2011a). The profiles also are consistent with resolved sources at other urban sites in China (e.g., Beijing, Shanghai, and Shenzhen) (He et al., 2011; Huang et al., 2012; Xu et al., 2015; Zhao et al., 2017). The distinction between LO-OOA and MO-OOA is their degree of oxidation (Xu et al., 2017), and larger ratio of *m/z* 44/43 was found for MO-OOA profile (8.5) compared with LO-OOA profile (1.9). Consistent with the lower degree of oxidation for LO-OOA, its correlations with hydrocarbon-like ions (e.g., $C_nH^+_{2n+1}$ and $C_nH^+_{2n-1}$) were stronger than those for MO-OOA. The fact that LO-OOA was less oxygenated (less aged) than MO-OOA, is probably because LO-OOA includes higher levels of more freshly emitted species than MO-OOA.

The diurnal pattern of LO-OOA for both periods showed an enhancement in the daytime (Fig. S13e), which were more than likely related to photochemical production. The LO-OOA peak during the lockdown period was lower and of shorter duration compared with the normal period. This difference was likely due to the reduction of organic precursors (e.g., volatile organic compounds (VOCs)) during the COVID-19 lockdown period. The MO-OOA correlated well with sulfate (Pearson's r = 0.75, Table S1), and that was likely caused by regional transport because the rates at which the two species form differ considerably (Huang et al., 2014). The diurnal profile of MO-OOA showed relative constant values during the normal period, but an obvious decrease was observed in the afternoon during the lockdown period (Fig. S13f); this indicates a reduced influence of regional transport when the restrictions on activities were put in place. Indeed, the average mass concentration of LO-OOA decreased from 8.6 ± 6.4 μg m^{-3} to 5.6 ± 3.7 μg m^{-3} from the normal period to the lockdown period, while MO-OOA decreased from 12.0 ± 4.9 μg m^{-3} to 9.5 ± 3.3 μg m^{-3} (Table 1). The total OOA (LO-OOA + MO-OOA) mass fraction of OA (51% during normal period and 56% during the COVID-19 lockdown period) was higher than that of POA (HOA + COA + CCOA + BBOA) (49% and 44%), highlighting the role of secondary OA formation in PM pollution in Xi'an, especially during the lockdown.

3.3. Formation of secondary aerosols

3.3.1. Photochemical oxidation

Photochemical oxidation is an important pathway for the formation of secondary aerosols during the daytime (Robinson et al., 2007; Link et al., 2017), and the intraday pattern of secondary species concentrations relative to background-corrected CO (ΔCO) can be used to assess secondary aerosol formation by eliminating the effects of changes in PBLH (Decarlo et al., 2010). Here, ΔCO was defined as the lowest 1.25th percentile of the CO data during the normal (0.12 ppm) and COVID-19 lockdown (0.14 ppm) periods (Kondo et al., 2006). To explore the formation processes, the correlations of secondary aerosol species/ΔCO ratios of the rising stage during the daytime (08:00–17:00) for each day (Fig. S15) and O_x mixing ratio (an indicator of photochemical oxidation degree) (Wood et al., 2010) was established. As shown in Fig. 5, nitrate/ΔCO, LO-OOA/ΔCO, and MO-OOA/ΔCO all showed linear increases with O_x mixing ratio (R^2 = 0.42–0.95) during both the normal and COVID-19 lockdown periods, suggesting the importance of photochemical oxidation for the formation of nitrate and OOAs. Larger increasing rates in LO-OOA/ΔCO (0.33–0.44 (μg m^{-3} ppm^{-1}) ppb^{-1}) compared with those in MO-OOA/ΔCO (0.04–0.09 (μg m^{-3} ppm^{-1}) ppb^{-1}) indicated that the formation of LO-OOA through photochemical oxidation was more efficient compared with MO-OOA.

It is noteworthy that the slopes of nitrate/ΔCO, LO-OOA/ΔCO, and MO-OOA/ΔCO relationships with O_x mixing ratios were greater during the COVID-19 lockdown period than the normal period. This difference can be explained by the greater atmospheric oxidation capacity during the lockdown period, which can be inferred from the higher fraction of O_3 relative to O_x during the lockdown. In contrast, sulfate/ΔCO did not increase with O_x mixing ratio during either the normal or lockdown periods. One explanation for the lack of a relationship is that ~96% of hourly O_3 mixing ratios were < 35 ppb, which may have been too low for efficient sulfate formation via photochemical oxidation (Fang et al., 2019).

3.3.2. Aqueous-phase reaction

Numerous studies have shown that aqueous-phase reaction is another important pathway for the formation of secondary aerosols (Xue et al., 2014; Jiang et al., 2019). In our study, the ALWC, which can be served as an indicator of aqueous-phase reaction (Ervens et al., 2011), showed a strong power-law relationship with RH (R^2 = 0.94, Fig. S16). The correlations of secondary aerosol species/ΔCO ratios of the rising stage during the nighttime (18:00–07:00 the next day) for each day (Fig. S15) and the corresponding ALWC was established to assess the

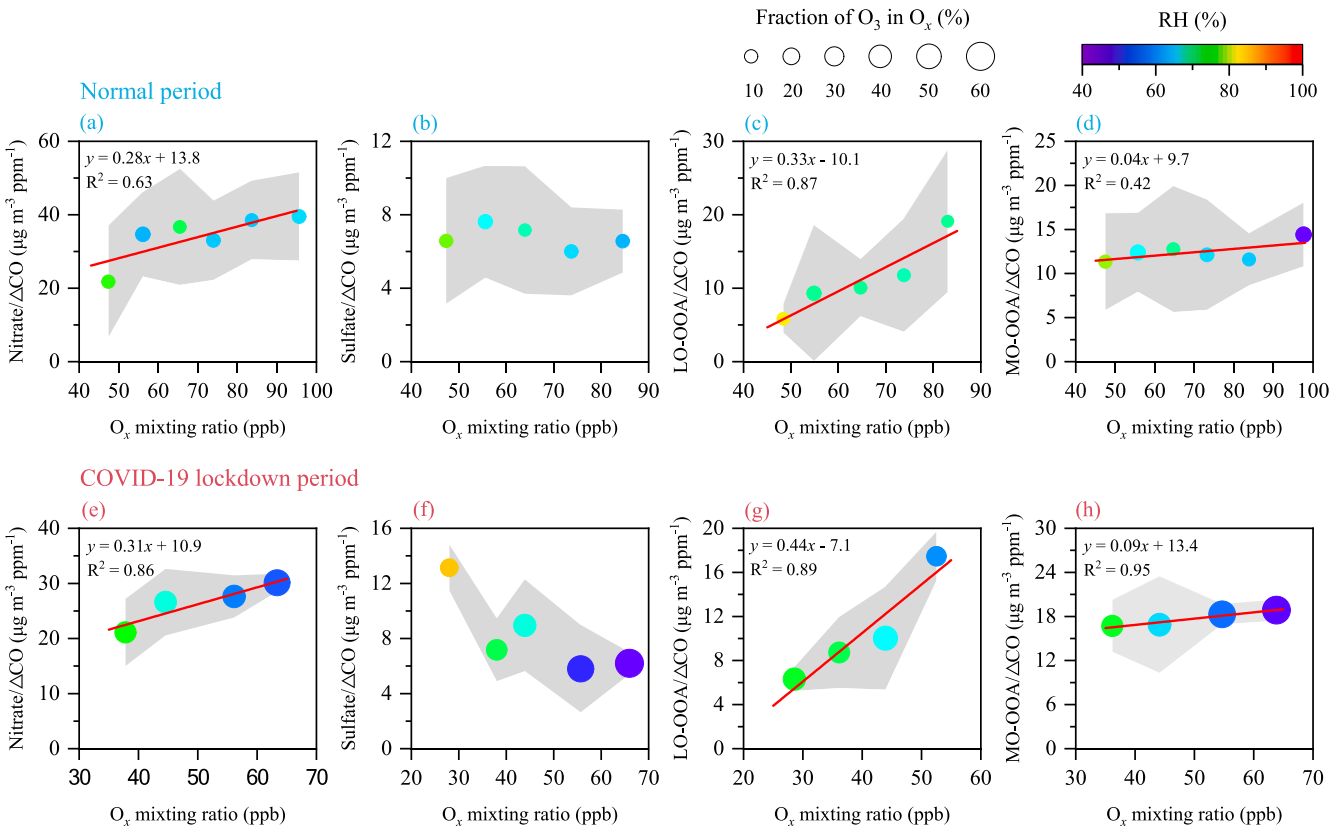

Fig. 5. Variations of nitrate/ΔCO, sulfate/ΔCO, LO-OOA/ΔCO, and MO-OOA/ΔCO ratios as a function of O_x mixing ratios during the (a–d) normal and (e–h) COVID-19 lockdown periods, respectively. The points and the light gray shadows represent the mean values and error margins of nitrate/ΔCO, sulfate/ΔCO, LO-OOA/ΔCO, and MO-OOA/ΔCO in each bin (ΔO_x = 10 ppb).

implications of aqueous-phase chemistry for aerosol production. As shown in Fig. 6, the formation of secondary species apparently varied as a function of RH. That is, when RH was less ~70–80%, all measured secondary species/ΔCO ratios showed obvious linear increases with ALWC (R^2 = 0.71–0.99), but the relationships changed when RH was higher than ~70–80%. For secondary inorganic species during the normal period, although increasing rates in nitrate/ΔCO and sulfate/ΔCO decreased from 0.64 (μg m^{-3} ppm^{-1}) (μg m^{-3})$^{-1}$ to 0.15 (μg m^{-3} ppm^{-1}) (μg m^{-3})$^{-1}$ and 0.13 (μg m^{-3} ppm^{-1}) (μg m^{-3})$^{-1}$ to 0.06 (μg m^{-3} ppm^{-1}) (μg m^{-3})$^{-1}$, respectively, when RH was > 80%, the positive correlations of these ratios with ALWC were still strong at RH > 80% (R^2 = 0.93–0.94). In contrast, LO-OOA/ΔCO and MO-OOA/ΔCO showed no obvious increases with ALWC at RH > 70%. This may be because the higher ALWC at RH > 70% inhibit secondary organic aerosol formation due to decreases in aerosol acidity (Huang et al., 2019; Meng et al., 2014). It is also noteworthy that at RH < 70%, the slopes of MO-OOA/ΔCO versus ALWC during both periods were higher than those of LO-OOA/ΔCO versus ALWC, indicating that the aqueous-phase reactions were more important for the formation of OOA with higher degrees of oxidation compared with the less oxidized species. Interestingly, Hu et al. (2016) concluded that MO-OOA in Beijing during the winter was mainly produced through photochemical processes.

Compared with the normal period, all secondary aerosol species/ΔCO ratios during the lockdown period showed larger increasing rates for similar ranges of RH. We note that nitrate (NO_3) radicals form through slow reactions of O_3 with NO_2, and they also can react rapidly with unsaturated species at night (Khan et al., 2008). The rate coefficient of the production reaction can be represented by $O_3 \times NO_2$, the latter being a proxy for the NO_3 radical. As shown in Fig. 6, the proxy was larger during the lockdown period than during the normal period, indicating the higher efficiency of NO_3 radical formation. Furthermore, the apparently higher formation efficiencies of nitrate/ΔCO, LO-OOA/ΔCO, and MO-OOA/ΔCO during the COVID-19 lockdown period was likely due to the increased abundances of the NO_3 radical, which could promote the formation of nitric acid and secondary organic aerosol (Brown et al., 2006; Hallquist et al., 2009; Li et al., 2020a). Meanwhile, aqueous-phase reactions when there was sufficient O_3 during the lockdown period may have promoted the formation of secondary sulfate aerosol (Meagher et al., 1990).

3.4. *Contrasting pollution episodes before and during the COVID-19 lockdown period*

Pollution episodes, defined as times when AQI > 100, occurred five during the normal period (EP1, EP2, EP3, EP4, and EP5) and three during the COVID-19 lockdown period (EP6, EP7, and EP8) (Fig. 1c). Due to the possible impacts of fireworks displays, including those on the Spring Festival Eve and the first two days (24 to 26 January) and the Lantern Festival (8 to 9 February), EP5 and EP8 were excluded from further analysis. As shown in Fig. 1, the wind speeds were quite stable and low (mean values: 0.47–0.70 m s^{-1}), and the prevailing winds were from the south to northwest for the EPs—these are conditions often associated with pollution events. For EP1, the sum of secondary inorganic aerosols (nitrate + sulfate + ammonium) accounted for 47% of PM mass on average, with nitrate showed the largest contribution (31%) (Fig. 7d). Meanwhile, OA contributed an average of 44% to the PM mass, and HOA was the largest contributor to OA (24%) (Fig. 7e). With reference to formation processes during EP1, the PM mass concentrations increased rapidly at rates of 16.4 μg m^{-3} h^{-1} from 00:00 to 10:00 on 3 January and 7.1 μg m^{-3} h^{-1} from 00:00 to 08:00 on 4 January, respectively (Fig. 1g). During these rapid increases in PM, the contributions of OA to PM mass exceeded those from secondary inorganic

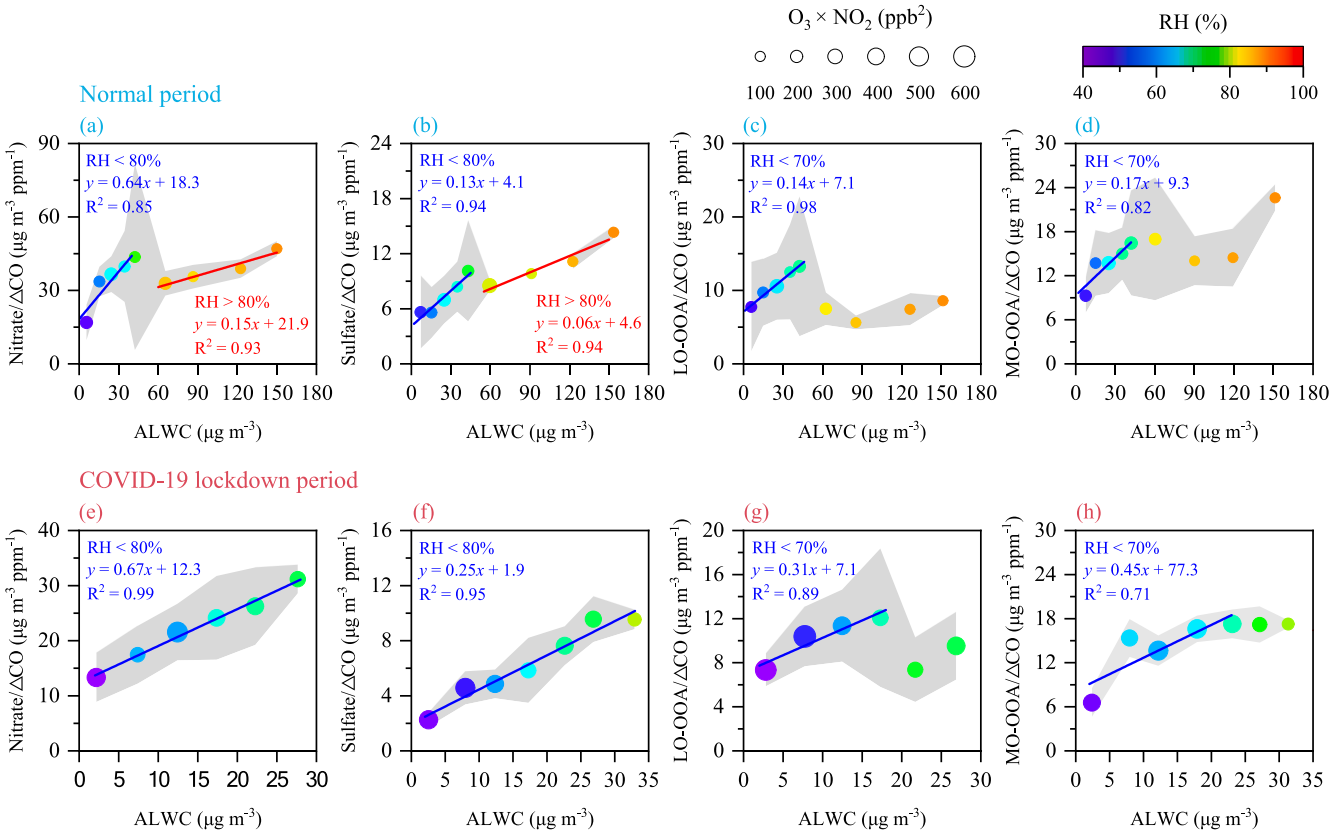

Fig. 6. Variations of nitrate/ΔCO, sulfate/ΔCO, LO-OOA/ΔCO, and MO-OOA/ΔCO ratios as a function of ALWC during the (a–d) normal and (e–h) COVID-19 lockdown periods, respectively. The points and light gray shadows represent the mean values and error margins in each bin. For the normal period, each bin was 10 μg m^{-3} (ΔALWC = 10 μg m^{-3}) when ALWC ranged from 0 to 50 μg m^{-3} but 30 μg m^{-3} (ΔALWC = 30 μg m^{-3}) for ALWC from 50 to 180 μg m^{-3} due to limitations in the data. For the COVID-19 lockdown period, each bin was 5 μg m^{-3} (ΔALWC = 5 μg m^{-3}).

aerosols; in fact, there were sharp increases in the relative loadings of POAs and LO-OOA. There results highlight the likelihood that primary emissions were a major cause for air pollution during the EP1.

Compared with EP1, the aerosol composition changed significantly for EP2, EP3, and EP4 during the normal period. All of those events also were in the normal period, and they showed higher secondary inorganic aerosols contributions (52–54%) compared with EP1 (Fig. 7d). The contribution of sulfate to PM increased about two-fold from EP1 to EP2–EP4, which is consistent with the higher SORs for those events. As shown in Fig. 1g, the concentrations of the three secondary inorganic species combined always were the most abundant of the aerosol constituents during these three pollution episodes. In addition, EP2–EP4 were characterized by the higher contributions of OOAs than POAs for OA (52–56% for OOAs; 44–48% for POAs), indicating strong secondary OA formation during the events. In particular, MO-OOA was the predominant contributor to OA (33–39%) which was much higher than that on the EP1 (23%). Due to the comparable oxidation conditions (small variability in O_x and low O_3 situation, Fig. 7b) for EP1 to EP4, the rapid increases in sulfate and MO-OOA on the EP2–EP4 were likely caused by aqueous-phase reactions that were favoured by relative high RH condition (71–79%, Fig. 7c); for comparison, the RH for EP1 was 56%.

Despite the restrictions on activities during the COVID-19 lockdown period, two pollution episodes occurred. For EP6 and EP7, the contributions of OA to PM (49–53%) were higher than that for the events during the normal period. In contrast, the contributions of secondary inorganic aerosols (40–44%) were smaller during the lockdown, apparently as a result of large decreases in precursors (see NO_x, Fig. 7a). Although the average values for O_x and ALWC were lower during EP6–EP7 than those in EP1 (Fig. 7b and c), the higher mass fractions of OOAs to OA (51–54%) were found during the EP6–EP7 than in EP1, and that can be explained by the greater atmospheric oxidation capacity (see discussion in Section 3.3). This finding is quite different from the results reported for Lanzhou city, that also was studied during the COVID-19 lockdown. In a study conducted there by Xu et al. (2020), the trends in secondary OA during the lockdown implied a lower atmospheric oxidation capacity. It is indicated that there are large differences in aerosol pollution chemistry in different cities when control measures were put in place. Air pollutions in both EP2–EP4 and EP6–EP7 were characterized by high contributions of OOAs, and this highlights the pervasive effects of secondary OA on air quality in the urban city. During those events, the OOA composition varied substantially, presumably in response to changes in photochemical oxidation and aqueous-phase reactions. The higher RH may have promoted aqueous-phase reactions that led to larger mass fractions of MO-OOA in EP2–EP4 relative to EP6–EP7. In contrast, stronger photochemical oxidation during the COVID-19 lockdown resulted in higher mass fractions of LO-OOA in EP6–EP7 (Fig. 7e) compared with EP2–EP4 during the normal period.

4. Conclusions

This study was conducted to investigate the composition of particulate matter (PM) (organic aerosol (OA), nitrate, sulfate, ammonium, chloride, and black carbon (BC)), the sources of OA, and the formation processes of secondary aerosols in the urban city of Xi'an, China before and during the COVID-19 lockdown period. The concentrations of PM and its species decreased dramatically during the lockdown period with reductions of 32–51%, and this is compelling evidence that restrictions on human activities led to lower PM loadings. The PM during both periods was mainly composed of OA, followed by nitrate, ammonium, sulfate, BC, and chloride, but the average contribution of OA to PM

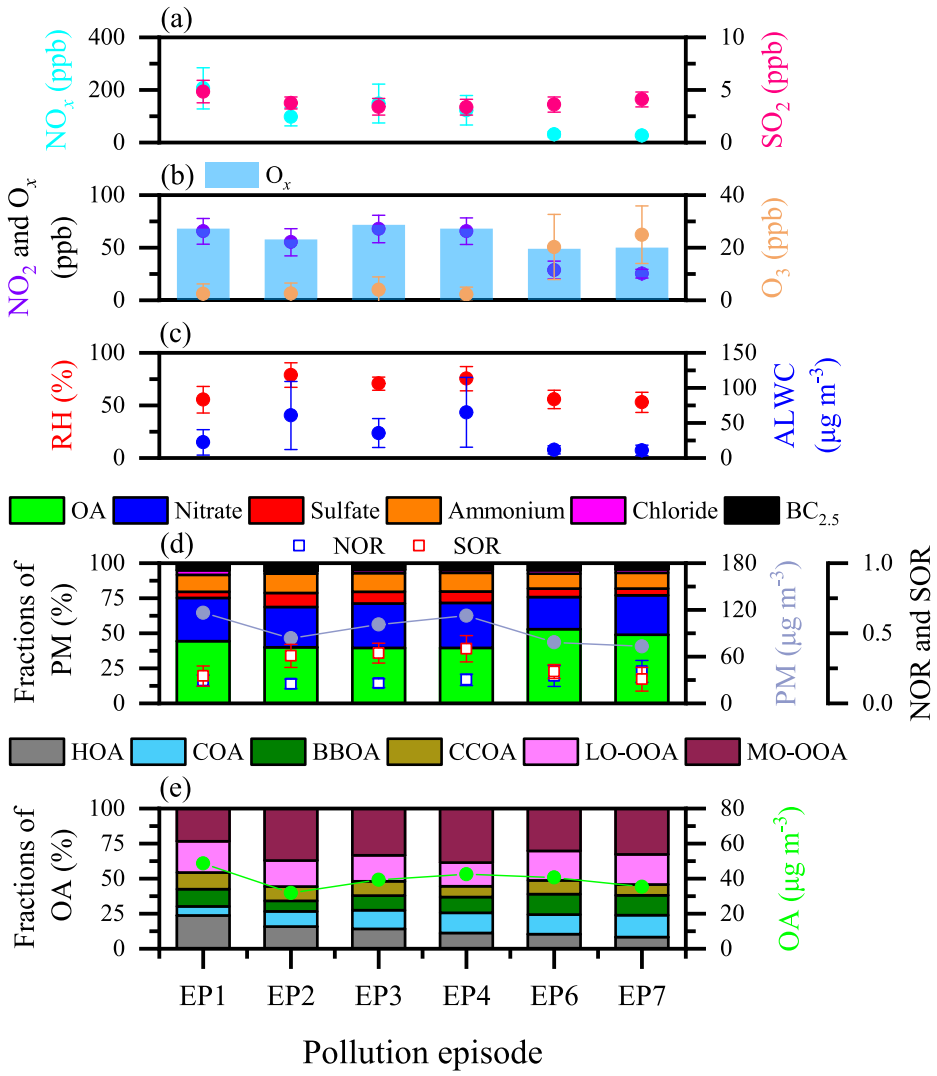

Fig. 7. Summary of gaseous pollutants, meteorological conditions, NOR, SOR, PM species, and OA composition for pollution episodes (EPs) during the normal and COVID-19 lockdown periods.

increased during the lockdown period. Moreover, the variations in aerosol composition relative to PM mass highlighted the increased importance of OA for air pollution during the lockdown period.

A hybrid environmental receptor model (HERM) was used to deconvolve the OA data into contributions from six factors: four primary OAs (POAs) (hydrocarbon-like OA (HOA), cooking OA (COA), biomass burning OA (BBOA), and coal combustion OA (CCOA)) and two oxygenated OAs (OOAs) (less-oxidized oxygenated OA (LO-OOA) and more-oxidized oxygenated OA (MO-OOA)). The mass concentrations of the POAs decreased by 17–58% after activities were restricted during the COVID-19 lockdown period. The HOA showed the largest reduction, and that can be explained by the strict restrictions placed on motor vehicle usage. Although the lockdown did reduce emissions from catering operations, the biomass burned in fields, and the use of coal by industries, the residential use of biomass and coal for heating and cooking were not restricted, resulting in the smaller declines in COA, BBOA, and CCOA compared with HOA. Furthermore, the mass concentrations of LO-OOA and MO-OOA decreased by 21–35%, whereas the OOA contributions to OA increased during the lockdown, indicating the enhanced secondary OA formation capacity during the COVID-19 lockdown period.

Finally, the correlations of secondary aerosol species/ΔCO ratios versus O_x (NO_2 + O_3) indicated that photochemical oxidation was an important process for the formation of nitrate and two OOAs. Meanwhile, all secondary aerosol species/ΔCO were strongly correlated with the aerosol liquid water content (ALWC) under a RH threshold of ~70–80%, reflecting the importance of aqueous-phase reactions. Increases in O_3 and NO_3 radical during the lockdown favoured the formation of secondary aerosols by increasing the atmospheric oxidation capacity. The analysis of pollution episodes (EPs) showed that OA instead of secondary inorganic species became the major contributor to air pollution formation during the COVID-19 lockdown period, especially the LO-OOA produced by photochemical oxidation process.

CRediT authorship contribution statement

Jie TiaHan: Writing - original draft, Writing - review & editing, Methodology, Formal analysis, Funding acquisition. **Qiyuan Wang:** Conceptualization, Methodology, Writing - review & editing, Supervision, Funding acquisition. **Yong Zhang:** Investigation. **Mengyuan Yan:** Investigation. **Huikun Liu:** Investigation. **Ningning Zhang:** Writing - review & editing. **Weikang Ran:** Investigation. **Junji Cao:** Conceptualization, Writing - review & editing, Supervision, Funding acquisition.

Declaration of Competing Interest

The authors declare that they have no known competing financial interests or personal relationships that could have appeared to influence the work reported in this paper.

Acknowledgements

This work was supported by the Key Research and Development Program of Shaanxi Province (2018-ZDXM3-01), the Sino-Swiss Cooperation on Air Pollution for Better Air (7F-09802.01.02), the Youth Innovation Promotion Association of the Chinese Academy of Sciences (2019402), the National Natural Science Foundation of China (NSFC 21661132005), the West Light Foundation of the Chinese Academy of Sciences (XAB2019B05), the National Atmospheric Research Program (2017YFC0212200), and the Key Deployment Program of the Chinese Academy of Sciences (ZDRW-ZS-2017-6). The authors are grateful to the staff from Guanzhong Plain, Eco-environmental Change and Comprehensive Treatment, National Observation and Research Station for their assistance with field sampling.

Appendix A. Supplementary material

Supplementary data to this article can be found online at https://doi.org/10.1016/j.envint.2021.106426.

References

Allan, J.D., Williams, P.I., Morgan, W.T., Martin, C.L., Flynn, M.J., Lee, J., Nemitz, E., Phillips, G.J., Gallagher, M.W., Coe, H., 2010. Contributions from transport, solid fuel burning and cooking to primary organic aerosols in two UK cities. Atmos. Chem. Phys. 10, 647–668. https://doi.org/10.5194/acp-10-647-2010.

Allan, J.D., Jimenez, J.L., Williams, P.I., Alfarra, M.R., Bower, K.N., Jayne, J.T., Coe, H., Worsnop, D.R., 2003. Quantitative sampling using an Aerodyne aerosol mass spectrometer – 1. Techniques of data interpretation and error analysis. J. Geophys. Res.-Atmos. 108, 4090. https://doi.org/10.1029/2002JD002358.

Brown, S.S., Ryerson, T.B., Wollny, A.G., Brock, C.A., Peltier, R., Sullivan, A.P., Weber, R. J., Dubé, W.P., Trainer, M., Meagher, J.F., Fehsenfeld, F.C., Ravishankara, A.R., 2006. Variability in nocturnal nitrogen oxide processing and its role in regional air quality. Science 311, 67–70. https://doi.org/10.1126/science.1120120.

Budisulistiorini, S.H., Canagaratna, M.R., Croteau, P.L., Baumann, K., Edgerton, E.S., Kollman, M.S., Ng, N.L., Verma, V., Shaw, S.L., Knipping, E.M., Worsnop, D.R., Jayne, J.T., Weber, R.J., Surratt, J.D., 2014. Intercomparison of an Aerosol Chemical Speciation Monitor (ACSM) with ambient fine aerosol measurements in downtown Atlanta Georgia. Atmos. Meas. Tech. 7, 1929–1941. https://doi.org/10.5194/amt-7-1929-2014.

Canonaco, F., Crippa, M., Slowik, J.G., Baltensperger, U., Prévôt, A.S.H., 2013. SoFi, an IGOR-based interface for the efficient use of the generalized multilinear engine (ME-2) for the source apportionment: ME-2 application to aerosol mass spectrometer data. Atmos. Meas. Tech. 6, 3649–3661. https://doi.org/10.5194/amt-6-3649-2013.

Cao, J.J., Lee, S.C., Ho, K.F., Zou, S.C., Fung, K., Li, Y., Watson, J.G., Chow, J.C., 2004. Spatial and seasonal variations of atmospheric organic carbon and elemental carbon in Pearl River Delta Region China. Atmos. Environ. 38, 4447–4456. https://doi.org/10.1016/j.atmosenv.2004.05.016.

Chen, L.W., Cao, J.J., 2018. $PM_{2.5}$ source apportionment using a hybrid environmental receptor model. Environ. Sci. Technol. 52, 6357–6369. https://doi.org/10.1021/acs.est.8b00131.

Crippa, M., DeCarlo, P.F., Slowik, J.G., Mohr, C., Heringa, M.F., Chirico, R., Poulain, L., Freutel, F., Sciare, J., Cozic, J., Di Marco, C.F., Elsasser, M., Nicolas, J.B., Marchand, N., Abidi, E., Wiedensohler, A., Drewnick, F., Schneider, J., Borrmann, S., Nemitz, E., Zimmermann, R., Jaffrezo, J.L., Prévôt, A.S.H., Baltensperger, U., 2013a. Wintertime aerosol chemical composition and source apportionment of the organic fraction in the metropolitan area of Paris. Atmos. Chem. Phys. 13, 961–981. https://doi.org/10.5194/acp-13-961-2013.

Crippa, M., El Haddad, I., Slowik, J.G., Decarlo, P.F., Mohr, C., Heringa, M.F., Chirico, R., Marchand, N., Sciare, J., Baltensperger, U., Prévôt, A.S.H., 2013b. Identification of marine and continental aerosol sources in Paris using high resolution aerosol mass spectrometry. J. Geophys. Res.-Atmos. 118, 1950–1963. https://doi.org/10.1002/jgrd.50151.

Cubison, M.J., Ortega, A.M., Hayes, P.L., Farmer, D.K., Day, D., Lechner, M.J., Brune, W. H., Apel, E., Diskin, G.S., Fisher, J.A., Fuelberg, H.E., Hecobian, A., Knapp, D.J., Mikoviny, T., Riemer, D., Sachse, G.W., Sessions, W., Weber, R.J., Weinheimer, A.J., Jimenez, J.L., 2011. Effects of aging on organic aerosol from open biomass burning smoke in aircraft and lab studies. Atmos. Chem. Phys. 11, 12049–12064. https://doi.org/10.5194/acpd-11-12103-2011.

Decarlo, P.F., Ulbrich, I.M., Crounse, J., de Foy, B., Dunlea, E.J., Aiken, A.C., Knapp, D., Weinheimer, A.J., Campos, T., Wennberg, P.O., Jimenez, J.L., 2010. Investigation of the sources and processing of organic aerosol over the Central Mexican Plateau from aircraft measurements during MILAGRO. Atmos. Chem. Phys. 10, 5257–5280. https://doi.org/10.5194/acp-10-5257-2010.

Drinovec, L., Močnik, G., Zotter, P., Prévôt, A.S.H., Ruckstuhl, C., Coz, E., Rupakheti, M., Sciare, J., Müller, T., Wiedensohler, A., Hansen, A.D.A., 2015. The "dual-spot" Aethalometer: an improved measurement of aerosol black carbon with real-time loading compensation. Atmos. Meas. Tech. 8, 1965–1979. https://doi.org/10.5194/amt-8-1965-2015.

Ervens, B., Turpin, B.J., Weber, R.J., 2011. Secondary organic aerosol formation in cloud droplets and aqueous particles (aqSOA): a review of laboratory, field and model studies. Atmos. Chem. Phys. 11, 11069–11102. https://doi.org/10.5194/acp-11-11069-2011.

Fang, Y.H., Ye, C.X., Wang, J.X., Wu, Y.S., Hu, M., Lin, W.L., Xu, F.F., Zhu, T., 2019. Relative humidity and O_3 concentration as two prerequisites for sulfate formation. Atmos. Chem. Phys. 19, 12295–12307. https://doi.org/10.5194/acp-19-12295-2019.

Feng, Y.Y., Ning, M., Lei, Y., Sun, Y.M., Liu, W., Wang, J., 2019. Defending blue sky in China: Effectiveness of the "Air Pollution Prevention and Control Action Plan" on air quality improvements from 2013 to 2017. J. Environ. Manage. 252, 109603 https://doi.org/10.1016/j.jenvman.2019.109603.

Fountoukis, C., Nenes, A., 2007. ISORROPIA II: a computationally efficient thermodynamic equilibrium model for K^+–Ca^{2+}–Mg^{2+}–NH_4^+–SO_4^{2-}–NO_3^-–Cl^-–H_2O aerosols. Atmos. Chem. Phys. 7, 4639–4659. https://doi.org/10.5194/acp-7-4639-2007.

Fröhlich, R., Crenn, V., Setyan, A., Belis, C.A., Canonaco, F., Favez, O., Riffault, V., Slowik, J.G., Aas, W., Aijälä, M., Alastuey, A., Artiñano, B., Bonnaire, N., Bozzetti, C., Bressi, M., Carbone, C., Coz, E., Croteau, P.L., Cubison, M.J., EsserGietl, J.K., Green, D.C., Gros, V., Heikkinen, L., Herrmann, H., Jayne, J.T., Lunder, C.R., Minguillón, M.C., Mocnik, G., O'Dowd, C.D., Ovadnevaite, J., Petralia, E., Poulain, L., Priestman, M., Ripoll, A., Sarda-Estève, R., Wiedensohler, A., Baltensperger, U., Sciare, J., Prévôt, A.S.H., 2015. ACTRIS ACSM intercomparison-Part 2: Intercomparison of ME-2 organic source apportionment results from 15 individual, co-located aerosol mass spectrometers. Atmos. Meas. Tech. 8, 2555–2576. https://doi.org/10.5194/amt-8-2555-2015.

Gao, J.J., Wang, K., Wang, Y., Liu, S.H., Zhu, C.Y., Hao, J.M., Liu, H.J., Hua, S.B., Tian, H. Z., 2017. Temporal-spatial characteristics and source apportionment of $PM_{2.5}$ as well as its associated chemical species in the Beijing-Tianjin-Hebei region of China. Environ. Pollut. 233, 714–724. https://doi.org/10.1016/j.envpol.2017.10.123.

Hallquist, M., Wenger, J.C., Baltensperger, U., Rudich, Y., Simpson, D., Claeys, M., Dommen, J., Donahue, N.M., George, C., Goldstein, A.H., Hamilton, J.F., Herrmann, H., Hoffmann, T., Iinuma, Y., Jang, M., Jenkin, M.E., Jimenez, J.L., Kiendler-Scharr, A., Maenhaut, W., McFiggans, G., Mentel, T.F., Monod, A., Prévôt, A.S.H., Seinfeld, J.H., Surratt, J.D., Szmigielski, R., Wildt, J., 2009. The formation, properties and impact of secondary organic aerosol: current and emerging issues. Atmos. Chem. Phys. 9, 5155–5236. https://doi.org/10.5194/acp-9-5155-2009.

Han, T.T., Xu, W.Q., Chen, C., Liu, X.G., Wang, Q.Q., Li, J., Zhao, X.J., Du, W., Wang, Z. F., Sun, Y.L., 2015. Chemical apportionment of aerosol optical properties during the Asia-Pacific Economic Cooperation summit in Beijing, China. J. Geophys. Res.-Atmos. 120, 12281–12295. https://doi.org/10.1002/2015JD023918.

He, L.Y., Huang, X.F., Xue, L., Hu, M., Lin, Y., Zheng, J., Zhang, R.Y., Zhang, Y.H., 2011. Submicron aerosol analysis and organic source apportionment in an urban atmosphere in Pearl River Delta of China using high-resolution aerosol mass spectrometry. J. Geophys. Res.-Atmos. 116, D12304. https://doi.org/10.1029/2010JD014566.

He, L.Y., Lin, Y., Huang, X.F., Guo, S., Xue, L., Su, Q., Hu, M., Luan, S.J., Zhang, Y.H., 2010. Characterization of high-resolution aerosol mass spectra of primary organic aerosol emissions from Chinese cooking and biomass burning. Atmos. Chem. Phys. 10, 11535–11543. https://doi.org/10.5194/acp-10-11535-2010.

Hu, W.W., Hu, M., Hu, W., Jimenez, J.L., Yuan, B., Chen, W.T., Wang, M., Wu, Y.S., Chen, C., Wang, Z.B., Peng, J.F., Zeng, L.M., Shao, M., 2016. Chemical composition, sources and aging process of sub-micron aerosols in Beijing: contrast between summer and winter. J. Geophys. Res.-Atmos. 121, 1955–1977. https://doi.org/10.1002/2015JD024020.

Huang, R.J., Zhang, Y., Bozzetti, C., Ho, K.F., Cao, J.J., Han, Y., Daellenbach, K.R., Slowik, J.G., Platt, S.M., Canonaco, F., Zotter, P., Wolf, R., Pieber, S.M., Bruns, E.A., Crippa, M., Ciarelli, G., Piazzalunga, A., Schwikowski, M., Abbaszade, G., Schnelle-Kreis, J., Zimmermann, R., An, Z.S., Szidat, S., Baltensperger, U., Haddad, I.E., Prévôt, A.S.H., 2014. High secondary aerosol contribution to particulate pollution during haze events in China. Nature 514, 218–222. https://doi.org/10.1038/nature13774.

Huang, X., Ding, A., Gao, J., Zheng, B., Zhou, D., Qi, X., Tang, R., Wang, J., Ren, C., Nie, W., Chi, X., Xu, Z., Chen, L., Li, Y., Che, F., Pang, N., Wang, H., Tong, D., Qin, W., Cheng, W., Liu, W., Fu, Q., Liu, B., Chai, F., Davis, J.S., Zhang, Q., He, K., 2020. Enhanced secondary pollution offset reduction of primary emissions during COVID-19 lockdown in China. Natl. Sci. Rev. https://doi.org/10.1093/nsr/nwaa137 nwaa137.

Huang, X.F., He, L.Y., Hu, M., Canagaratna, M.R., Sun, Y., Zhang, Q., Zhu, T., Xue, L., Zeng, L.W., Liu, X.G., Zhang, Y.H., Jayne, J.T., Ng, N.L., Worsnop, D.R., 2010. Highly time-resolved chemical characterization of atmospheric submicron particles during 2008 Beijing Olympic Games using an Aerodyne High-Resolution Aerosol Mass Spectrometer. Atmos. Chem. Phys. 10, 8933–8945. https://doi.org/10.5194/acp-10-8933-2010.

Huang, X.F., He, L.Y., Xue, L., Sun, T.L., Zeng, L.W., Gong, Z.H., Hu, M., Zhu, T., 2012. Highly time-resolved chemical characterization of atmospheric fine particles during

2010 Shanghai World Expo. Atmos. Chem. Phys. 12, 4897–4907. https://doi.org/10.5194/acp-12-4897-2012.
Huang, X.J., Zhang, J.K., Luo, B., Luo, J.Q., Zhang, W., Rao, Z.H., 2019. Characterization of oxalic acid-containing particles in summer and winter seasons in Chengdu. China. Atmos. Environ. 198, 133–141. https://doi.org/10.1016/j.atmosenv.2018.10.050.
Jiang, H.H., Frie, A.L., Lavi, A., Chen, J.Y., Zhang, H., Bahreini, R., Lin, Y.-H., 2019. Brown carbon formation from nighttime chemistry of unsaturated heterocyclic volatile organic compounds. Environ. Sci. Technol. Lett. 6, 184–190. https://doi.org/10.1021/acs.estlett.9b00017.
Khan, M.A.H., Ashfold, M.J., Nickless, G., Martin, D., Watson, L.A., Hamer, P.D., Wayne, R.P., Canosa-Mas, C.E., Shallcross, D.E., 2008. Night-time NO_3 and OH radical concentrations in the United Kingdom inferred from hydrocarbon measurements. Atmos. Sci. Lett. 9, 140–146. https://doi.org/10.1002/asl.175.
Kim, H., Zhang, Q., Bae, G.N., Kim, J.Y., Lee, S.B., 2017. Sources and atmospheric processing of winter aerosols in Seoul, Korea: Insights from real-Time measurements using a high-resolution aerosol mass spectrometer. Atmos. Chem. Phys. 17, 2009–2033. https://doi.org/10.5194/acp-17-2009-2017.
Kirchstetter, T.W., Thatcher, T.L., 2012. Contribution of organic carbon to wood smoke particulate matter absorption of solar radiation. Atmos. Chem. Phys. 12, 6067–6072. https://doi.org/10.5194/acp-12-6067-2012.
Kondo, Y., Komazaki, Y., Miyazaki, Y., Moteki, N., Takegawa, N., Kodama, D., Deguchi, S., Nogami, M., Fukuda, M., Miyakawa, T., Morino, Y., Koike, M., Sakurai, H., Ehara, K., 2006. Temporal Variations of elemental carbon in Tokyo. J. Geophys. Res. 111, D12205. https://doi.org/10.1029/2005jd006257.
Lanz, V.A., Alfarra, M.R., Baltensperger, U., Buchmann, B., Hueglin, C., Prévôt, A.S.H., 2007. Source apportionment of submicron organic aerosols at an urban site by factor analytical modelling of aerosol mass spectra. Atmos. Chem. Phys. 7, 1503–1522. https://doi.org/10.5194/acp-7-1503-2007.
Le, T.H., Wang, Y., Liu, L., Yang, J.N., Yung, Y., Li, G.H., Seinfeld, J.H., 2020. Unexpected air pollution with marked emission reductions during the COVID-19 outbreak in China. Science. https://doi.org/10.1126/science.abb7431.
Li, C.L., He, Q.F., Hettiyadura, A.P.S., Käfer, U., Shmul, G., Meidan, D., Zimmermann, R., Brown, S.S., George, C., Laskin, A., Rudich, Y., 2020a. Formation of secondary brown carbon in biomass burning aerosol proxies through NO_3 radical reactions. Environ. Sci. Technol. 54, 1395–1405. https://doi.org/10.1021/acs.est.9b05641.
Li, H.Y., Zhang, Q., Zhang, Q., Chen, C.R., Wang, L.T., Wei, Z., Zhou, S., Parworth, C., Zheng, B., Canonaco, F., Prévôt, A.S.H., Chen, P., Zhang, H.L., Wallington, T.J., He, K.B., 2017. Wintertime aerosol chemistry and haze evolution in an extremely polluted city of the North China Plain: significant contribution from coal and biomass combustion. Atmos. Chem. Phys. 17, 4751–4768. https://doi.org/10.5194/acp-17-4751-2017.
Li, L., Li, Q., Huang, L., Wang, Q., Zhu, A.S., Xu, J., Liu, Z.Y., Li, H.L., Shi, L.S., Li, R., Azari, M., Wang, Y.J., Zhang, X.J., Liu, Z.Q., Zhu, Y.H., Zhang, K., Xue, S.H., Ooi, M. C.G., Zhang, D.P., Chan, A., 2020b. Air quality changes during the COVID-19 lockdown over the Yangtze River Delta Region: An insight into the impact of human activity pattern changes on air pollution variation. Sci. Total Environ. 732, 139282 https://doi.org/10.1016/j.scitotenv.2020.139282.
Lin, C.S., Ceburnis, D., Hellebust, S., Buckley, P., Wenger, J., Canonaco, F., Prévôt, A.S. H., Huang, R.J., O'Dowd, C., Ovadnevaite, J., 2017. Characterization of primary organic aerosol from domestic wood, peat, and coal burning in Ireland. Environ. Sci. Technol. 51, 10624–10632. https://doi.org/10.1021/acs.est.7b01926.
Link, M.F., Kim, J., Park, G., Lee, T., Park, T., Babar, Z.B., Sung, K., Kim, P., Kang, S., Kim, J.S., Choi, Y., Son, J., Lim, H.-J., Farmer, D.K., 2017. Elevated production of NH_4NO_3 from the photochemical processing of vehicle exhaust: Implications for air quality in the Seoul Metropolitan Region. Atmos. Environ. 156, 95–101. https://doi.org/10.1016/j.atmosenv.2017.02.031.
Liu, Y.H., Ma, J.L., Li, L., Lin, X.F., Xu, W.J., Ding, H., 2018. A high temporal-spatial vehicle emission inventory based on detailed hourly traffic data in a medium-sized city of China. Environ. Pollut. 236, 324–333. https://doi.org/10.1016/j.envpol.2018.01.068.
Ma, T., Duan, F.K., He, K.B., Qin, Y., Tong, D., Geng, G., Liu, X., Li, H., Yang, S., Ye, S.Q., Xu, B.Y., Zhang, Q., Ma, Y.L., 2019. Air pollution characteristics and their relationship with emissions and meteorology in the Yangtze River Delta region during 2014–2016. J. Environ. Sci. 83, 8–20. https://doi.org/10.1016/j.jes.2019.02.031.
Meagher, J.F., Olszyna, K.J., Weatherford, F.P., Mohnen, V.A., 1990. The availability of H_2O_2 and O_3 for aqueous phase oxidation of SO_2: The question of linearity. Atmos. Environ. 24, 1825–1829. https://doi.org/10.1016/0960-1686(90)90514-N.
Meng, J., Wang, G., Li, J., Cheng, C., Ren, Y., Huang, Y., Cheng, Y., Cao, J., Zhang, T., 2014. Seasonal characteristics of oxalic acid and related SOA in the free troposphere of Mt. Hua, central China: implications for sources and formation mechanisms. Sci. Total Environ. 493, 1088–1097.
Ministry of Environmental Protection of the People' Republic of China (MEE), 2012. Technical Regulation on Ambient Air Quality Index (On Trial), HJ633-2012, available at: http://www.mee.gov.cn/ywgz/fgbz/bz/bzwb/jcffbz/201203/W020120410332725219541.pdf.
Middlebrook, A.M., Bahreini, R., Jimenez, J.L., Canagaratna, M.R., 2012. Evaluation of composition-dependent collection efficiencies for the Aerodyne Aerosol Mass Spectrometer using field data. Aerosol Sci. Technol. 46, 258–271. https://doi.org/10.1080/02786826.2011.620041.
Mohr, C., DeCarlo, P.F., Heringa, M.F., Chirico, R., Slowik, J.G., Richter, R., Reche, C., Alastuey, A., Querol, X., Seco, R., Peñuelas, J., Jiménez, J.L., Crippa, M., Zimmermann, R., Baltensperger, U., Prévôt, A.S.H., 2012. Identification and quantification of organic aerosol from cooking and other sources in Barcelona using aerosol mass spectrometer data. Atmos. Chem. Phys. 12, 1649–1665. https://doi.org/10.5194/acp-12-1649-2012.
Ng, N.L., Canagaratna, M.R., Jimenez, J.L., Chhabra, P.S., Seinfeld, J.H., Worsnop, D.R., 2011a. Changes in organic aerosol composition with aging inferred from aerosol mass spectra. Atmos. Chem. Phys. 11, 6465–6474. https://doi.org/10.5194/acp-11-6465-2011.
Ng, N.L., Canagaratna, M.R., Jimenez, J.L., Zhang, Q., Ulbrich, I.M., Worsnop, D.R., 2011b. Real-time methods for estimating organic component mass concentrations from Aerosol Mass Spectrometer Data. Environ. Sci. Technol. 45, 910–916. https://doi.org/10.1021/es102951k.
Ng, N.L., Herndon, S.C., Trimborn, A., Canagaratna, M.R., Croteau, P.L., Onasch, T.B., Sueper, D., Worsnop, D.R., Zhang, Q., Sun, Y.L., Jayne, J.T., 2011c. An Aerosol Chemical Speciation Monitor (ACSM) for routine monitoring of the composition and mass concentrations of ambient aerosol. Aerosol Sci. Technol. 45, 780–794. https://doi.org/10.1080/02786826.2011.560211.
Niu, X.Y., Cao, J.J., Shen, Z.X., Ho, S.S.H., Tie, X.X., Zhao, S.Y., Xu, H.M., Zhang, T., Huang, R.J., 2016. $PM_{2.5}$ from the Guanzhong Plain: Chemical composition and implications for emission reductions. Atmos. Environ. 147, 458–469. https://doi.org/10.1016/j.atmosenv.2016.10.029.
Paatero, P., Tapper, U., 1994. Positive matrix factorization: A non-negative factor model with optimal utilization of error estimates of data values. Environmetrics 5, 111–126. https://doi.org/10.1002/env.3170050203.
Reyes-Villegas, E., Bannan, T.J., Le Breton, M., Mehra, A., Priestley, M., Percival, C., Coe, H., Allan, J., 2018. Online chemical characterization of food-cooking organic aerosols: Implications for source apportionment. Environ. Sci. Technol. 52, 5308–5318. https://doi.org/10.1021/acs.est.7b06278.
Robinson, A.L., Donahue, N.M., Shrivastava, M.K., Weitkamp, E.A., Sage, A.M., Grieshop, A.P., Lane, T.E., Pierce, J.R., Pandis, S.N., 2007. Rethinking organic aerosols: Semivolatile emissions and photochemical aging. Science. 315, 1259–1262. https://doi.org/10.1126/science.1133061.
Sun, Y.L., Du, W., Fu, P.Q., Wang, Q.Q., Li, J., Ge, X.L., Zhang, Q., Zhu, C.M., Ren, L.J., Xu, W.Q., Zhao, J., Han, T.T., Worsnop, D.R., Wang, Z.F., 2016. Primary and secondary aerosols in Beijing in winter: sources, variations andprocesses. Atmos. Chem. Phys. 16, 8309–8329. https://doi.org/10.5194/acp-16-8309-2016.
Sun, Y.L., Jiang, Q., Wang, Z.F., Fu, P.Q., Li, J., Yang, T., Yin, Y., 2014. Investigation of the sources and evolution processes of severe haze pollution in Beijing in January 2013. J. Geophys. Res. -Atmos. 119, 4380–4398. https://doi.org/10.1002/2014JD021641.
Sun, Y.L., Wang, Z.F., Fu, P.Q., Yang, T., Jiang, Q., Dong, H.B., Li, J., Jia, J.J., 2013. Aerosol composition, sources and processes during wintertime in Beijing. China. Atmos. Chem. Phys. 13, 4577–4592. https://doi.org/10.5194/acp-13-4577-2013.
Sun, Y.L., Zhang, Q., Schwab, J.J., Demerjian, K.L., Chen, W.N., Bae, M.S., Huang, H.M., Hogrefe, O., Frank, B., Rattigan, O.V., Lin, Y.C., 2011. Characterization of the sources and processes of organic and inorganic aerosols in New York City with a high-resolution time-of-flight aerosol mass spectrometer. Atmos. Chem. Phys. 11, 1581-1602. http://doi.org /10.5194/acp-11-1581-2011.
Ulbrich, I.M., Canagaratna, M.R., Zhang, Q., Worsnop, D.R., Jimenez, J.L., 2009. Interpretation of organic components from Positive Matrix Factorization of aerosol mass spectrometric data. Atmos. Chem. Phys. 9, 2891–2918. https://doi.org/10.5194/acp-9-2891-2009.
Wang, J.F., Ge, X.L., Chen, Y.F., Shen, Y.F., Zhang, Q., Sun, Y.L., Xu, J.Z., Ge, S., Yu, H., Chen, M., 2016. Highly time-resolved urban aerosol characteristics during springtime in Yangtze River Delta, China: Insights from soot particle aerosol mass spectrometry. Atmos. Chem. Phys. 16, 9109–9127. https://doi.org/10.5194/acp-16-9109-2016.
Wang, P., Cao, J.J., Shen, Z.X., Han, Y.M., Lee, S.C., Huang, Y., Zhu, C.S., Wang, Q.Y., Xu, H.M., Huang, R.J., 2015. Spatial and seasonal variations of $PM_{2.5}$ mass and species during 2010 in Xi'an. China. Sci. Total Environ. 508, 477–487. https://doi.org/10.1016/j.scitotenv.2014.11.007.
Wang, P.F., Chen, K.Y., Zhu, S.Q., Wang, P., Zhang, H.L., 2020a. Severe air pollution events not avoided by reduced anthropogenic activities during COVID-19 outbreak. Resour. Conserv. Recycl. 158, 104814 https://doi.org/10.1016/j.resconrec.2020.104814.
Wang, Y.C., Huang, R.J., Ni, H.Y., Chen, Y., Wang, Q.Y., Li, G.H., Tie, X.X., Shen, Z.X., Huang, Y., Liu, S.X., Dong, W.M., Xue, P., Fröhlich, R., Canonaco, F., Elser, M., Daellenbach, K.R., Bozzetti, C., El Haddad, I., Prévôt, A.S.H., Canagaratna, M.R., Worsnop, D.R., Cao, J.J., 2017. Chemical composition, sources and secondary processes of aerosols in Baoji city of northwest China. Atmos. Environ. 158, 128–137. https://doi.org/10.1016/j.atmosenv.2017.03.026.
Wang, Y.C., Wang, Q.Y., Ye, J.H., Li, L., Zhou, J., Ran, W.K., Zhang, R.J., Wu, Y.F., Cao, J.J., 2020b. Chemical composition and sources of submicron aerosols in winter at a regional site in Beijing-Tianjin-Hebei region: Implications for the Joint Action Plan. Sci. Total Environ. 719, 137547 https://doi.org/10.1016/j.scitotenv.2020.137547.
Wang, Y.C., Yuan, Y., Wang, Q.Y., Liu, C.G., Zhi, Q., Cao, J.J., 2020c. Changes in air quality related to the control of coronavirus in China: Implications for traffic and industrial emissions. Sci. Total Environ. 731, 139133 https://doi.org/10.1016/j.scitotenv.2020.139133.
Wood, E.C., Canagaratna, M.R., Herndon, S.C., Onasch, T.B., Kolb, C.E., Worsnop, D.R., Kroll, J.H., Knighton, W.B., Seila, R., Zavala, M., Molina, L.T., DeCarlo, P.F., Jimenez, J.L., Weinheimer, A.J., Knapp, D.J., Jobson, B.T., Stutz, J., Kuster, W.C., Williams, E.J., 2010. Investigation of the correlation between odd oxygen and secondary organic aerosol in Mexico City and Houston. Atmos. Chem. Phys. 10, 8947–8968. https://doi.org/10.5194/acp-10-8947-2010.
Xu, J., Ge, X., Zhang, X., Zhao, W., Zhang, R., Zhang, Y., 2020. COVID-19 impact on the concentration and composition of submicron particulate matter in a typical city of Northwest China. Geophys. Res. Lett. 47, e2020GL089035. https://doi.org/10.1029/2020GL089035.

Xu, W.Q., Han, T.T., Du, W., Wang, Q.Q., Chen, C., Zhao, J., Zhang, Y.J., Li, J., Fu, P.Q., Wang, Z.F., Worsnop, D.R., Sun, Y.L., 2017. Effects of aqueous-phase and photochemical processing on secondary organic aerosol formation and evolution in Beijing. China. Environ. Sci. Technol. 51, 762–770. https://doi.org/10.1021/acs.est.6b04498.

Xu, W.Q., Sun, Y.L., Chen, C., Du, W., Han, T.T., Wang, Q.Q., Fu, P.Q., Wang, Z.F., Zhao, X.J., Zhou, L.B., Ji, D.S., Wang, P.C., Worsnop, D.R., 2015. Aerosol composition, oxidation properties, and sources in Beijing: results from the 2014 Asia-Pacific Economic Cooperation summit study. Atmos. Chem. Phys. 15, 23407–23455. https://doi.org/10.5194/acp-15-13681-2015.

Xue, J., Griffith, S.M., Yu, X., Lau, A.K.H., Yu, J.Z., 2014. Effect of nitrate and sulfate relative abundance in $PM_{2.5}$ on liquid water content explored through half-hourly observations of inorganic soluble aerosols at a polluted receptor site. Atmos. Environ. 99, 24–31. https://doi.org/10.1016/j.atmosenv.2014.09.049.

Yang, S., Ma, Y.L., Duan, F.K., He, K.B., Wang, L.T., Wei, Z., Zhu, L.D., Ma, T., Li, H., Ye, S.Q., 2017. Characteristics and formation of typical winter haze in Handan, one of the most polluted cities in China. Sci. Total Environ. 613–614, 1367–1375. https://doi.org/10.1016/j.scitotenv.2017.08.033.

Zhang, J.K., Wang, L.L., Wang, Y.H., Wang, Y.S., 2016. Submicron aerosols during the Beijing Asia-Pacific Economic Cooperation conference in 2014. Atmos. Environ. 124, 224–231. https://doi.org/10.1016/j.atmosenv.2015.06.049.

Zhang, Q., Zheng, Y.X., Tong, D., Shao, M., Wang, S.X., Zhang, Y.H., Xu, X.D., Wang, J. N., He, H., Liu, W.Q., Ding, Y.H., Lei, Y., Li, J.H., Wang, Z.F., Zhang, X.Y., Wang, Y. S., Cheng, J., Liu, Y., Shi, Q.R., Yan, L., Geng, G.N., Hong, C.P., Li, M., Liu, F., Zheng, B., Cao, J.J., Ding, A.J., Gao, J., Fu, Q.Y., Huo, J.T, Liu, B.X., Liu, Z.R., Yang, F.M., He, K.B., Hao, J.M., 2019. Drivers of improved PM2.5 air quality in China from 2013 to 2017. Proc. Natl. Acad. Sci. U.S.A. 116, 24463. https://doi.org/10.1073/pnas.1907956116.

Zhang, R., Jing, J., Tao, J., Hsu, S.C., Wang, G., Cao, J., Lee, C.S.L., Zhu, L., Chen, Z., Zhao, Y., Shen, Z., 2013. Chemical characterization and source apportionment of $PM_{2.5}$ in Beijing: seasonal perspective. Atmos. Chem. Phys. 13, 7053–7074. https://doi.org/10.5194/acp-13-7053-2013.

Zhang, R.Y., Wang, G.H., Guo, S., Zamora, M.L., Ying, Q., Lin, Y., Wang, W.G., Hu, M., Wang, Y., 2015. Formation of Urban Fine Particulate Matter. Chem. Rev. 115, 3803–3855. https://doi.org/10.1021/acs.chemrev.5b00067.

Zhang, T., Cao, J.J., Chow, J.C., Shen, Z.X., Ho, K.F., Ho, S.S.H., Liu, S.X., Han, Y.M., Watson, J.G., Wang, G.H., Huang, R.J., 2014. Characterization and seasonal variations of levoglucosan in fine particulate matter in Xi'an. China. J. Air Waste Manage. Assoc. 64, 1317–1327. https://doi.org/10.1080/10962247.2014.944959.

Zhang, T., Cao, J.J., Tie, X.X., Shen, Z.X., Liu, S.X., Ding, H., Han, Y.M., Wang, G.H., Ho, K.F., Qiang, J., Li, W.T., 2011. Water-soluble ions in atmospheric aerosols measured in Xi'an, China: seasonal variations and sources. Atmos. Res. 102, 110–119. https://doi.org/10.1016/j.atmosres.2011.06.014.

Zhao, J., Du, W., Zhang, Y.J., Wang, Q.Q., Chen, C., Xu, W.Q., Han, T.T., Wang, Y.Y., Fu, P.Q., Wang, Z.F., Li, Z.Q., Sun, Y.L., 2017. Insights into aerosol chemistry during the 2015 China Victory Day parade: results from simultaneous measurements at ground level and 260 m in Beijing. Atmos. Chem. Phys. 17, 3215–3232. https://doi.org/10.5194/acp-17-3215-2017.

Zhao, Y.B., Zhang, K., Xu, X.T., Shen, H.Z., Zhu, X., Zhang, Y.X., Hu, Y.T., Shen, G.F., 2020. Substantial changes in nitrogen dioxide and ozone after excluding meteorological impacts during the COVID-19 Outbreak in mainland China. Environ. Sci. Technol. Lett. 7, 402–408. https://doi.org/10.1021/acs.estlett.0c00304.

Zheng, B., Tong, D., Li, M., Liu, F., Hong, C.P., Geng, G.N., Li, H.Y., Li, X., Peng, L.Q., Qi, J., Yan, L., Zhang, Y.X., Zhao, H.Y., Zheng, Y.X., He, K.B., Zhang, Q., 2018. Trends in China's anthropogenic emissions since 2010 as the consequence of clean air actions. Atmos. Chem. Phys. 18, 14095–14111. https://doi.org/10.5194/acp-18-14095-2018.

Zheng, H., Kong, S.F., Chen, N., Yan, Y.Y., Liu, D.T., Zhu, B., Xu, K., Cao, W.X., Ding, Q. Q., Lan, B., Zhang, Z.X., Zheng, M.M., Fan, Z.W., Cheng, Y., Zheng, S.R., Yao, L.Q., Bai, Y.Q., Zhao, T.L., Qi, S.H., 2020. Significant changes in the chemical compositions and sources of $PM_{2.5}$ in Wuhan since the city lockdown as COVID-19. Sci. Total Environ. 739, 140000 https://doi.org/10.1016/j.scitotenv.2020.140000.

Zheng, S., Cao, C.X., Singh, R.P., 2014. Comparison of ground based indices (API and AQI) with satellite based aerosol products. Sci. Total Environ. 488–489, 398–412. https://doi.org/10.1016/j.scitotenv.2013.12.074.

Zhou, W., Jiang, J., Duan, L., Hao, J., 2016. Evolution of submicrometer organic aerosols during a complete residential coal combustion process. Environ. Sci. Technol. 50, 7861–7869. https://doi.org/10.1021/acs.est.6b00075.